Cardiolipin externalization to the outer mitochondrial membrane acts as an elimination signal for mitophagy in neuronal cells

Charleen T. Chu[1,12], Jing Ji[2,3,4,5,10], Ruben K. Dagda[1,10,11], Jian Fei Jiang[2,3,10], Yulia Y. Tyurina[2,3], Alexandr A. Kapralov[2,3], Vladimir A. Tyurin[2,3], Naveena Yanamala[6], Indira H. Shrivastava[7], Dariush Mohammadyani[6,11], Kent Zhi Qiang Wang[1], Jianhui Zhu[1], Judith Klein-Seetharaman[6,11], Krishnakumar Balasubramanian[2,3], Andrew A. Amoscato[2,3], Grigory Borisenko[2,3], Zhentai Huang[2,3], Aaron M. Gusdon[1], Amin Cheikhi[2,3], Erin K. Steer[1], Ruth Wang[1], Catherine Baty[8,9], Simon Watkins[8,9], Ivet Bahar[7], Hülya Bayır[2,3,4,5,12] and Valerian E. Kagan[2,3,12]

Recognition of injured mitochondria for degradation by macroautophagy is essential for cellular health, but the mechanisms remain poorly understood. Cardiolipin is an inner mitochondrial membrane phospholipid. We found that rotenone, staurosporine, 6-hydroxydopamine and other pro-mitophagy stimuli caused externalization of cardiolipin to the mitochondrial surface in primary cortical neurons and SH-SY5Y cells. RNAi knockdown of cardiolipin synthase or of phospholipid scramblase-3, which transports cardiolipin to the outer mitochondrial membrane, decreased the delivery of mitochondria to autophagosomes. Furthermore, we found that the autophagy protein microtubule-associated-protein-1 light chain 3 (LC3), which mediates both autophagosome formation and cargo recognition, contains cardiolipin-binding sites important for the engulfment of mitochondria by the autophagic system. Mutation of LC3 residues predicted as cardiolipin-interaction sites by computational modelling inhibited its participation in mitophagy. These data indicate that redistribution of cardiolipin serves as an 'eat-me' signal for the elimination of damaged mitochondria from neuronal cells.

Mitochondria are indispensable for aerobic life in eukaryotic cells; yet injured or dysfunctional mitochondria generate reactive oxygen species (ROS) and release mediators that kill cells. In response, eukaryotic cells developed mechanisms to sequester and degrade mitochondria through macroautophagy. Although once thought of as a non-selective bulk degradation process, the selective recognition of dysfunctional mitochondria for mitochondrial autophagy (mitophagy) has recently been established[1–4]. Yet, molecular signals underlying recognition of injured mitochondria remain incompletely defined[3,4], particularly in neurons, and mammals lack the adaptor proteins identified in yeast[2]. Mitochondria, like their bacterial ancestors, contain in their inner
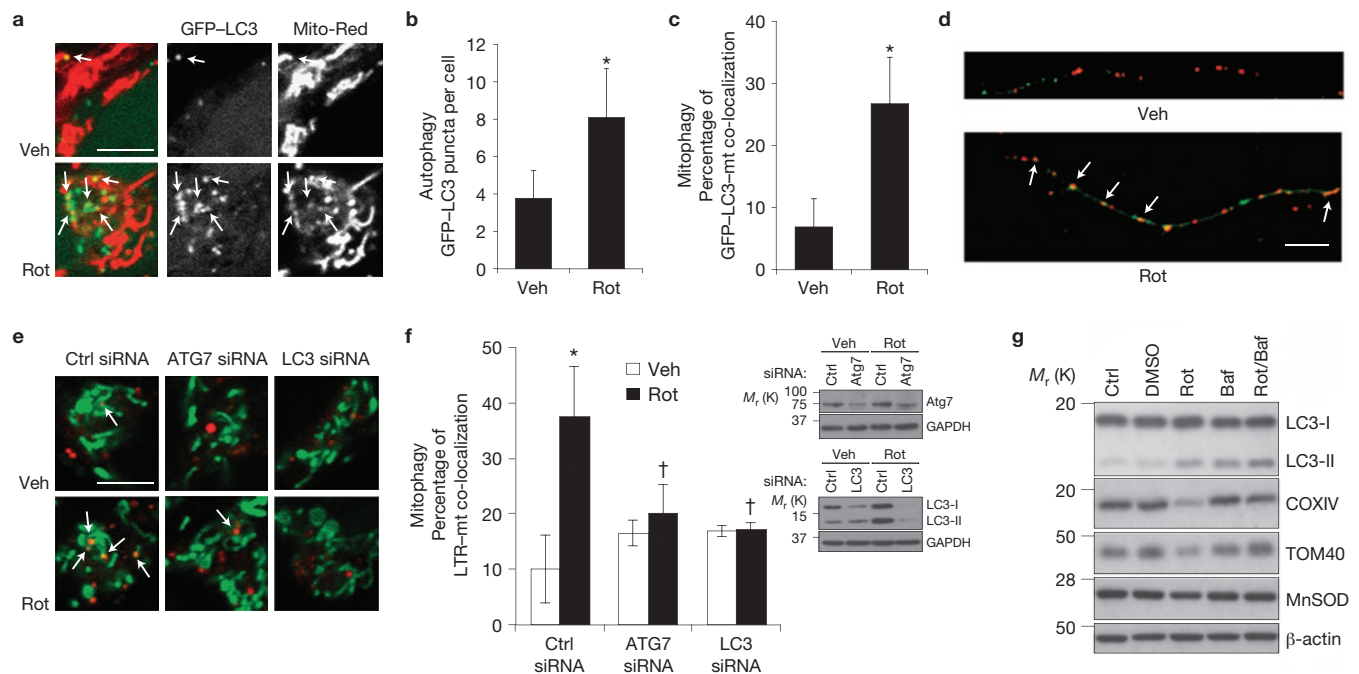
membrane the phospholipid cardiolipin[5] (CL), which is not found in any other organelle. Here, we provide evidence that the recognition of this ancient phospholipid serves an important defensive function for the elimination of damaged mitochondria in both primary and transformed neuronal cells.

In healthy mitochondria, CL is localized to the inner mitochondrial membrane (IMM), where it interacts with proteins to support cristae, stabilize respiratory chain complexes[6], and modulate autophagy and cell death[7]. The unique structure of CL includes a compact, negatively charged head group, whereas mammalian LC3 contains basic surface patches[8]. Just as the collapse of plasma membrane phosphatidylserine

1197

Figure 1 Rotenone-induced mitophagy. (**a–d**) Rotenone (Rot) increased the number of GFP–LC3 puncta and the level of co-localization with mitochondria (arrows) in SH-SY5Y cells (**a–c**; 1 μM) and primary cortical neurons (**d**; 250 nM), quantified in Fig. 3f and Supplementary Fig. S1b,c. Veh, vehicle. (**e,f**) Rotenone increased delivery of MitoTracker Green-stained mitochondria (mt) to LysoTracker Red (LTR)-stained lysosomes, inhibited by siRNA knockdown of ATG7 or LC3 in SH-SY5Y cells. Ctrl, control. Right: RNAi knockdown. (**g**) Rotenone decreased IMM (COXIV), OMM (TOM40) and matrix (MnSOD) protein expression levels in primary neurons, reversed by bafilomycin (Baf) inhibition of autolysosomal degradation, quantified in Supplementary Fig. S1e. Mean ± s.d. of $n = 7$ independent experiments for **b,c**, and $n = 3$ independent experiments for **f,g** (see Supplementary Table S4 for statistics source data); *$P < 0.05$ versus vehicle control; †$P < 0.05$ versus Rot/control siRNA. Scale bars, 10 μm. See Supplementary Fig. S7 for uncropped blots.

asymmetry serves an important signalling function for phagocytosis[9], we investigated the hypothesis that CL externalization to the outer mitochondrial membrane (OMM) acts as an elimination signal for mitophagy in mammalian cells.

RESULTS

Rotenone elicits increased autophagy and mitophagy

Disruptions in mitophagy are centrally implicated in neurodegenerative diseases and ageing[10–12]. Mitophagy was elicited in primary rat cortical neurons and SH-SY5Y neuroblastoma cells using the complex I inhibitor rotenone (Fig. 1) under sublethal or prelethal conditions (Supplementary Fig. S1a). The ubiquitin-fold domain of LC3 is involved in a lipidation reaction by which LC3 is covalently bound to autophagic membranes, and LC3 puncta are used as specific markers of autophagosomes[13]. Rotenone elicited increases in GFP–LC3 puncta (Fig. 1a,b and Supplementary Fig. S1b) and in the percentage of GFP–LC3 puncta co-localizing with mitochondria (Fig. 1c,d and Supplementary Fig. S1c), indicating a preferential increase in mitophagosomes relative to total autophagosomes.

Rotenone induced a decrease in p62 (SQSMT1) levels, consistent with increased autophagic flux (Supplementary Fig. S1d). Co-localization of mitochondria with LysoTracker Red confirmed maturation and delivery of cargo to lysosomes, which was inhibited by small interfering RNA (siRNA) knockdown of the autophagy proteins ATG7 or LC3 (Fig. 1e,f). The loss of mitochondrial proteins from the IMM, OMM and matrix subcompartments was reversed by co-treatment with bafilomycin to prevent autophagosome–lysosome

fusion[13] (Fig. 1g and Supplementary Fig. S1e). Likewise, sublethal staurosporine (STS) treatments elicited mitophagy in primary neurons (Supplementary Fig. S1f–h) and in SH-SY5Y cells, reversed by siRNA knockdown of ATG7 or LC3 (Supplementary Fig. S1i).

CL translocates to the mitochondrial outer surface in response to pro-mitophagy stimuli

To analyse the mitochondrial redistribution of CL during mitophagy, we purified and characterized OMM and IMM fractions (Supplementary Fig. S2a,b) from mitochondria isolated from rotenone- or STS-treated neurons, and measured the levels of CL by quantitative liquid chromatography–mass spectrometry (LC–MS). Rotenone treatment increased both the total content and the numbers of individual molecular species of CL detected in the OMM fraction (Fig. 2a and Table 1). Under basal conditions, ∼0.8% of CL resides in the OMM fraction from cortical neurons. Rotenone elicited an ∼10-fold increase in CL content in the OMM, whether the data were normalized to mitochondrial protein (Table 1), or to total mitochondrial lipid phosphorus (Fig. 2b). There were no major changes in the spectra for the other major mitochondrial phospholipids (Supplementary Fig. S2c). Phosphatidic acid (PA) is another anionic phospholipid present in mitochondrial membranes. We found that the OMM content of PA was increased, but to a lesser extent than CL (Table 1). STS-treated neurons showed similar changes (Fig. 2b and Table 1).

Neuronal CLs are comprised of multiple species resolvable by LC–MS, sharing the same head group, but with different fatty acyl chains. Control MS spectra for CL exhibited 7 IMM and 4 OMM CL
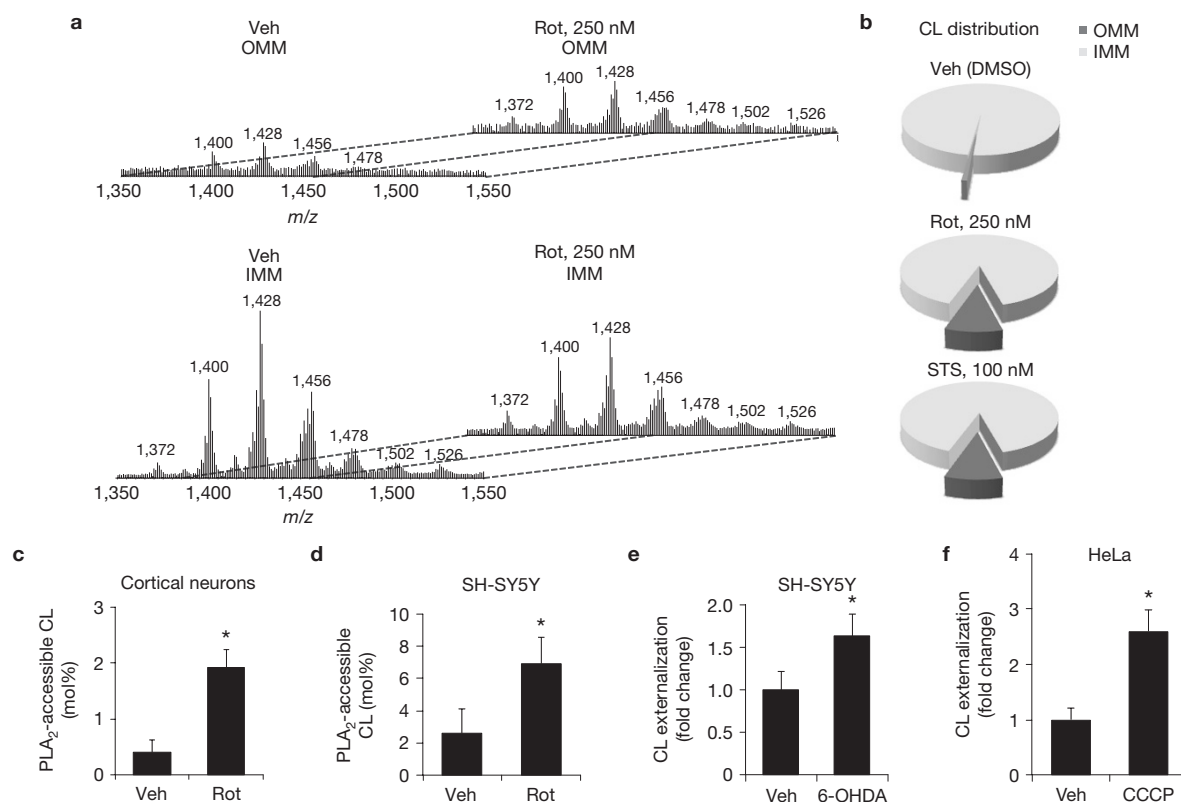
Figure 2 Analysis of mitochondrial CL distribution and externalization. (**a,b**) IMM and OMM fractions isolated from primary neurons following the indicated treatments were lipid extracted for LC–MS analysis. (**a**) MS spectra demonstrated increased cardiolipin (CL) content of the OMM after rotenone (Rot) treatment, with diversification of the cluster distribution to the 7 clusters exhibited by the IMM. Veh, vehicle. (**b**) Pie charts showing the CL distribution between IMM and OMM fractions from toxin-treated neurons, normalized to mitochondrial lipid phosphorus. (**c,d**) Treatment with rotenone caused significant increases in PLA$_2$-hydrolysable (surface accessible) CL assessed by LC–MS in primary cortical neurons (**c**; 250 nM) and SH-SY5Y cells (**d**; 1 μM). (**e,f**) Treatment with 6-OHDA and CCCP increased surface exposure of CL probed with annexin V in SH-SY5Y (**e**, 120 μM) and parkin-expressing HeLa cells (**f**, 20 μM), respectively. Mean ± s.d. of $n = 3$ independent experiments for **c–f** (see Supplementary Table S4 for statistics source data); *$P < 0.05$ versus vehicle control.

clusters, whereas rotenone-treated samples exhibited 7 clusters for both IMM and OMM fractions (Fig. 2a). Fatty acyl chain analysis revealed an identical distribution of fatty acids in the most abundant species of each cluster (Supplementary Table S1), suggesting redistribution of pre-existing CL molecular species without fatty acyl chain remodelling. Notably, no increased CL peroxidation products were detected under these early, mitophagy-inducing treatment conditions involving low doses of rotenone or STS, in contrast to the well-documented increases in lipid oxidation that occur during apoptosis[14].

To determine whether CL was exposed to the outer surface of the OMM, and is not simply enriched owing to increased isolation of IMM–OMM contact sites, we employed several techniques. Western blot analysis showed no detectable contamination of OMM fractions by adenine nucleotide translocase, an IMM contact site protein[15] (Supplementary Fig. S2b). We also developed two quantitative assays that do not involve biochemical fractionation. Intact mitochondria isolated from control and treated cultures were incubated with anionic phospholipid-selective phospholipase A$_2$ (PLA$_2$), and the CL hydrolysis products monolyso-CL were quantified. Treatment with rotenone caused significant increases in surface-accessible CL in primary cortical neurons and in SH-SY5Y cells (Fig. 2c,d). In contrast, lyso-PA was not detected. Alternatively, we incubated intact, isolated mitochondria with fluorescently labelled annexin V, which binds CL especially well

among anionic phospholipids at <300 μM calcium concentrations (Supplementary Fig. S2d)[16]. Increased annexin V binding to isolated, intact mitochondria occurred not only in response to rotenone (Fig. 3a) and STS (Supplementary Fig. S2e), but also in other well-established models of mitophagy: 6-hydroxydopamine (6-OHDA) treatment of SH-SY5Y cells[17] and carbonylcyanide-3-chlorophenylhydrazone (CCCP)-treatment of parkin (also known as PARK2)-expressing HeLa cells[3] (Fig. 2e,f and Supplementary Fig. S5g). 6-OHDA injury is fully reversible at the early time point studied[18]. Thus, CL externalization and mitophagy occur before commitment to cell death in response to multiple injury stimuli.

CL externalization is important for cargo recognition during mitophagy

To determine whether the redistribution of CL was important for mitophagy, we knocked down human phospholipid scramblase-3 (PLS3; Supplementary Fig. S3a,b), a mitochondrial enzyme responsible for the translocation of CL from the IMM to the OMM (ref. 19). PLS3 knockdown prevented the rotenone-induced increase in CL exposure to the mitochondrial surface (Fig. 3a), inhibited the increase in GFP–LC3 mitochondrial co-localization without affecting autophagy induction (Fig. 3b,c), and inhibited the autophagic delivery of mitochondria to lysosomes and loss of mitochondrial proteins (Supplementary

Table 1 Content of CL and PA in IMM and OMM fractions of rat cortical neurons treated with rotenone or STS.

	Vehicle		Rotenone (250 nM, 2 h)		STS (100 nM, 2 h)	
	PL (nmol mg^{-1} protein)		PL (nmol mg^{-1} protein)		PL (nmol mg^{-1} protein)	
	IMM	OMM	IMM	OMM	IMM	OMM
CL	48.1 ± 0.9	0.4 ± 0.1 (0.82%)	46.6 ± 0.5	5.0 ± 0.1 (9.69%)	39.5 ± 1.0	4.2 ± 0.2 (9.61%)
PA	1.7 ± 0.2	0.2 ± 0.1 (10.53%)	2.0 ± 0.1	1.3 ± 0.1 (39.39%)	3.4 ± 0.2	1.2 ± 0.1 (26.09%)

Primary cortical neurons were isolated from day 16 embryonic rats, pooled and cultured. Primary cortical neurons (7–9 days *in vitro*) were treated with rotenone or STS for 2 h followed by isolation of IMM and OMM fractions as described in the Methods. Lipids were extracted and CL or PA identified and quantified by LC–MS analysis using ion trap and quadropole time-of-flight platforms. Results are expressed as the mean $\pm$ s.d. of $n = 5$ determinations. The percentage of the phospholipid (PL) present in the OMM fraction is shown in parentheses.

Fig. S3c,d). Similar effects were observed for 6-OHDA (Fig. 3d and Supplementary Fig. S3e) and STS (Supplementary Fig. S1i). PLS3 RNA-mediated interference (RNAi) did not cause significant changes in mitochondrial membrane potential (Supplementary Fig. S3f) in the presence or absence of rotenone. The effects of PLS3 RNAi in human SH-SY5Y cells were recapitulated using a second siRNA (Fig. 3d and Supplementary Fig. S3g), and reversed by overexpression of mouse PLS3 (Fig. 3e).

To further confirm a role for CL in the recognition of injured mitochondria for mitophagy in primary neurons, we used RNAi against CL synthase (CLS). Mammalian cells tolerate reductions to ∼45% of total CL without adverse effects on bioenergetics, membrane potential or ROS (refs 20,21). In primary neurons, CLS RNAi reduced CL levels to 57% ±1.4 at 72 h post-transfection. CLS knockdown using two distinct siRNAs (Supplementary Fig. S4a,d) diminished rotenone-induced mitophagy (Fig. 3f,g,i and Supplementary Figs S1c and S4c), with little or no effect on general autophagy (Fig. 3h and Supplementary Fig. S1b). CLS knockdown also prevented STS-induced loss of mitochondrial proteins (Supplementary Fig. S1f) and reduced mitochondrial co-localization with GFP–LC3 puncta (Supplementary Fig. S1h), with no significant effects on LC3-II shift (Supplementary Fig. S1f) or the overall number of GFP–LC3 puncta elicited (Supplementary Fig. S1g). Although CLS knockdown could affect other aspects of mitochondria or ER biology, there were no significant effects on the basal or rotenone-induced mitochondrial membrane potential (Supplementary Fig. S4b,f) or ATP levels, which remained at 96.5% ±16 of control levels. Taken together with the LC3 mutagenesis studies described below, these data support a role for CL in cargo selection in response to several mitophagy-inducing stimuli.

CL has been reported to bind several proteins, including the carboxy-terminal domain of the autophagy protein beclin 1 (ref. 22), the immunity-related GTPase IRGM (ref. 7) and the voltage-dependent anion channel (VDAC), which is implicated in depolarization-induced mitophagy[23,24]. As full-length beclin 1 does not interact with membranes[22], we examined whether the beclin 1 C-terminal domain could be involved. However, cleavage of beclin 1 to form the C-terminal fragment[25] was not observed under the sublethal or prelethal conditions used in this study to elicit mitophagy (Fig. 4a–c). Thus, it is unlikely that this interaction contributes to mitochondrial targeting to the autophagosome in these contexts.

Parkinsonian toxins initiate mitophagy through distinct mechanisms from FCCP/CCCP

Mitochondrial uncoupling agents such as the protonophores carbonyl cyanide-*p*-trifluoromethoxyphenylhydrazone (FCCP) or CCCP trigger depolarization-induced increases in PINK1 accumulation accompanied by parkin translocation to mitochondria[26–28]. In contrast, rotenone caused no more than 10–14% decreases of mitochondrial membrane potential in neurons and SH-SY5Y cells (Supplementary Figs S3f and S4b,f). Moreover, there was no evidence of increased PINK1 levels (Fig. 4d) nor of parkin translocation to mitochondria in the rotenone or 6-OHDA models (Fig. 4e), in agreement with a previous study contrasting the effects of strong depolarizing agents such as CCCP with the Parkinsonian neurotoxins MPP+ and 6-OHDA (ref. 29). Furthermore, the LC3- and ubiquitin-interacting protein p62 (SQSMT1), which has been variably implicated in parkin-mediated mitophagy[24,30], was not recruited to mitochondria in response to rotenone or 6-OHDA (Fig. 4f–h). Thus, the initiation steps elicited by rotenone and 6-OHDA seem to differ from those reported for FCCP or CCCP.

Using FCCP or CCCP as applied to SH-SY5Y cells or parkin-expressing HeLa cells, we found that CL-modulating RNAi treatments did not prevent depolarization-induced PINK1 stabilization or parkin translocation to the mitochondria (Supplementary Fig. S5a–c,f). Interestingly, as observed above, CCCP treatment did elicit CL externalization (Fig. 2f and Supplementary Fig. S5g,h), albeit to a lesser extent (∼2-fold) than observed in rotenone-treated neurons. Moreover, CL-modulating RNAi treatments partially suppressed mitochondrial co-localization with autophagosomes without affecting overall LC3 puncta formation (Supplementary Fig. S5d,e), and partially inhibited the loss of mitochondrial proteins elicited by CCCP (Supplementary Fig. S5i, see Supplementary Fig. S5j,k for validation of human CLS knockdown). Overexpression of the fission protein dynamin-related protein 1 (Drp1) did not rescue the inhibition of mitophagy by PLS3 knockdown (Supplementary Fig. S5e), suggesting that CL may act downstream of Drp1. These data raise the possibility of pathway convergence downstream of PINK1 or parkin, and or activation of dual pathways by CCCP.

CL interacts directly with LC3 for cargo recognition during mitophagy

Mechanisms of selective autophagy are just beginning to emerge[3,4]. LC3 serves as a receptor for cargo adapters that bind protein aggregates[31], and its homologue Atg8 functions in an analogous role in yeast[2]. Examination of the crystal structure of LC3 reveals basic patches at its surface that are not present in the related proteins GABARAP and GATE16 (ref. 8). Using a gel retardation assay, we found that recombinant LC3 can directly bind CL liposomes to a much greater extent than to phosphatidylcholine-only liposomes (Fig. 5a). We also found that LC3 interacts more favourably with CL containing four acyl chains, than with lyso-CLs, as evidenced by the ratio of phospholipid to LC3 that caused a 50% loss of the LC3 monomeric form entering the gel (IC$_{50}$; Fig. 5b). IC$_{50}$ analysis indicates that LC3 shows a stronger affinity
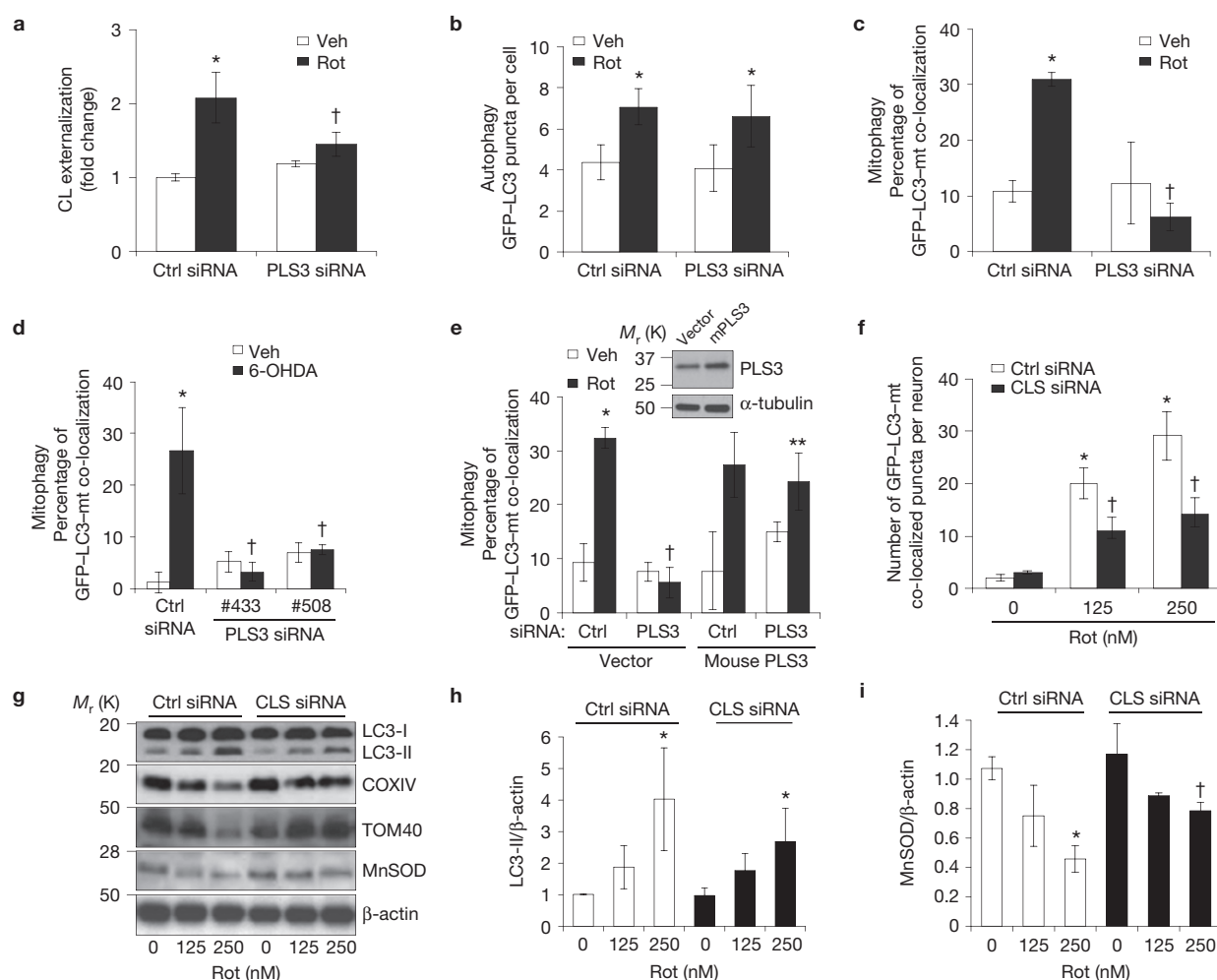
Figure 3 RNAi knockdown of CL enzymes attenuates CL exposure and mitophagy. (a–e) SH-SY5Y cells expressing control (Ctrl) or scramblase-3 siRNA #508 (PLS3 siRNA) for 72 h were stained with MitoTracker Green FM, a transmembrane potential-independent dye, and treated with rotenone (Rot; 1 μM). Veh, vehicle. (a) Anionic phospholipids exposed to the outer surface of isolated mitochondria were quantified by flow cytometry for Alexa 647–annexin V binding. (b–d) PLS3 knockdown had no effect on rotenone-induced autophagy (b), but decreased mitophagy in SH-SY5Y cells treated with rotenone (c; 1 μM) or 6-OHDA (d; 120 μM). (d,e) The effects of PLS3 siRNA were recapitulated using a second siRNA #433 (d, Supplementary Fig. S3b,g), and reversed by transfection with an RNAi-resistant mouse PLS3 vector (e). Inset: PLS3 overexpression. (f–i) Primary neurons transfected for 72 h with CLS siRNA or scrambled control siRNA were treated with rotenone (250 nM) and analysed for autophagy (Supplementary Fig. S1b) or mitophagy by either co-localization analysis (f), or with mitochondrial protein immunoblotting (g) and densitometry (h,i and Supplementary Fig. S4c). Knockdown efficiencies are shown in Supplementary Figs S3 and S4. Mean ± s.d. of $n = 4$ independent experiments for **b,c**, and $n = 3$ independent experiments for **a,d–f,h–i** (see Supplementary Table S4 for statistics source data); *$P < 0.05$ versus vehicle; †$P < 0.05$ versus toxin-treated control siRNA; **$P < 0.05$ versus Rot/PLS3 siRNA. See Supplementary Fig. S7 for uncropped blots.

for CL than for PA or phosphatidylglycerol (Fig. 5b), supported also by computational molecular dynamics simulations described below (Supplementary Fig. S6d).

Analysis of all existing protein crystal structures in complex with CL indicated that side-chain or backbone nitrogen atoms from lysine, arginine or histidine residues are required for stabilizing the phosphate moieties in CL. Molecular docking analysis predicts CL-binding pockets at the LC3 surface, where arginine and lysine interact with the sterically constrained head group of CL with two possible conformations (Fig. 5c,d). The top-ranked conformation involves stabilization of both CL phosphate groups (Fig. 5c), resulting in the lowest binding energy. The predicted coordinating amino acids (Fig. 5e) include N-terminal residues of LC3 such as Arg 10 and Arg 11 for the top-ranked conformation or Gln 26 and His 27

for the alternative conformation. Short-duration (100 ns) all-atom and longer 1,000 ns coarse-grained molecular dynamics simulations also implicate Arg 10 and Arg 11 in the initial interactions of LC3 with CL-containing membranes (Supplementary Fig. S6, Note and Table S2). The C terminus of LC3, which becomes crosslinked to autophagosome membranes, is predicted to remain exposed to solvent by coarse-grained modelling (Supplementary Fig. S6e, arrow), compatible with its proposed bridging role.

To test the ability of the N-terminal segment of LC3 to bind CL, we employed custom-synthesized 30-amino-acid peptides corresponding to the N-terminal sequence of wild-type LC3 or with substitution of leucines at Arg 10 and Arg 11. We determined their binding with CL-containing liposomes using the gel retardation assay. After native gel electrophoresis, 69.4 ± 9.7% and 102.4 ± 13.0% ($n = 8$, $p < 0.001$)
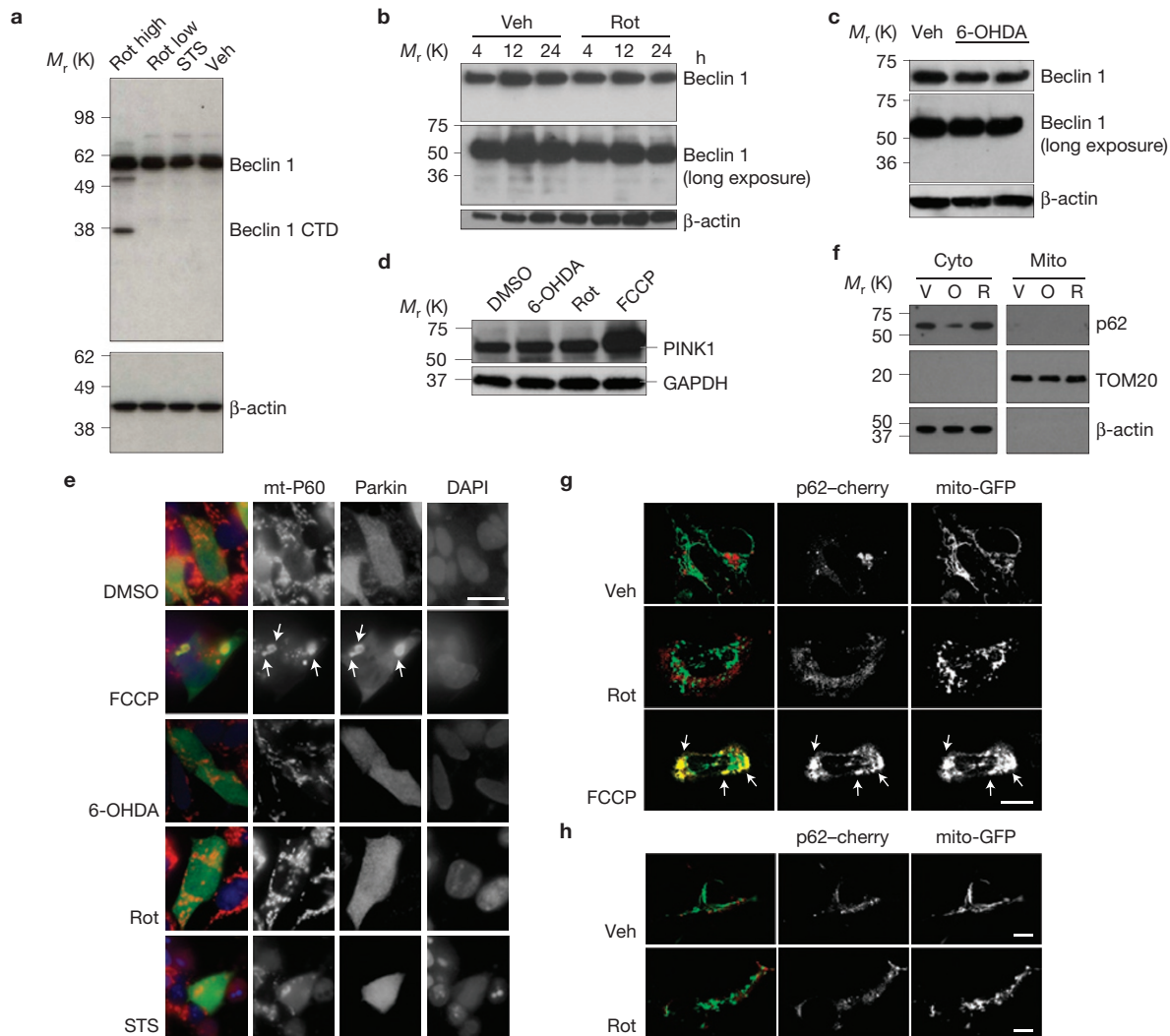
Figure 4 Effects of rotenone, STS or 6-OHDA on beclin 1 cleavage and distribution of parkin and p62. (**a**) Western blot analysis showed beclin 1 cleavage products ($<M_r$49 K) were not observed in primary neurons exposed to mitophagy-inducing sublethal concentrations of rotenone (250 nM × 2 h: Rot low) or STS (100 nM × 2 h). However, beclin 1 was cleaved on exposure to a lethal dose of rotenone (1 mM × 24 h: Rot high). Veh, vehicle; CTD, C-terminal domain. (**b,c**) Likewise, SH-SY5Y cells did not show beclin 1 cleavage on exposure to rotenone (**b**) or 6-OHDA (**c**; duplicate lanes). Data are representative of 2–3 independent experiments per toxin. (**d**) Cell lysates from stable PINK1-Flag-expressing SH-SY5Y cells were treated with 6-OHDA (120 μM), rotenone (1 μM) or FCCP (2 μM), and analysed by Flag immunoblot for PINK1–Flag levels. (**e**) SH-SY5Y cells transfected with HA–parkin were treated with the indicated toxins, immunolabelled for HA (green) and mitochondrial p60 antigen (red) and analysed for HA–parkin redistribution to mitochondria. FCCP elicited translocation of parkin to mitochondria (arrows), which was not seen with the other mitophagy stimuli. (**f**) Cytosolic and mitochondrial pellets were prepared from SH-SY5Y cells treated with vehicle (V), 6-OHDA (O, 120 μM) or rotenone (R, 1 μM). Gels were loaded with cytosolic or mitochondrial proteins, and immunoblotted for p62/SQSMT1, and the indicated fractionation markers. (**g,h**) Confocal analysis of p62/SQSMT1 distribution in SH-SY5Y cells (**g**) and in primary cortical neurons (**h**) that were co-transfected with mCherry-tagged p62/SQSMT1 and mitochondrially targeted GFP. Note recruitment of p62 to large mitochondrial aggregates (**g**, yellow, arrows) in FCCP-treated cells, which was not observed in control or rotenone-treated cells. Scale bars, 10 μm. See Supplementary Fig. S7 for uncropped blots.

of wild-type and mutant LC3, respectively, were detectable as unbound peptide, indicating that these residues, which are highly conserved among vertebrates (Supplementary Table S3), are important for the ability of LC3 to bind CL.

To establish experimentally key sites of contact between LC3 and CL, we deleted the N-terminal amino acids 1–28 predicted by molecular docking analysis to contain a major portion of the CL binding site (Fig. 5e), and analysed the ability of this LC3 mutant to participate in autophagy or mitophagy. Consistent with reports that the N-terminal α-helices are not essential for LC3 conjugation during non-selective autophagy[32], mutant LC3 participated equivalently to

wild-type LC3 in rapamycin-induced autophagy (Fig. 5f), but there was a tendency for reduced participation in response to rotenone or 6-OHDA (Fig. 5g,i). Strikingly, loss of the N-terminal α-helices abolished the ability of GFP–LC3 to undergo rotenone or 6-OHDA-induced co-localization with mitochondria (Fig. 5h,j). To test the involvement of two possible CL-binding regions predicted by docking analysis, we produced double point mutants of LC3 in which either Arg 10 and Arg 11 or Gln 26 and His 27 were mutated. The Arg 10 and Arg 11 mutation fully recapitulated the effects of deleting the α-helices, preventing the injury-induced increase in co-localization with mitochondria (Fig. 5k).
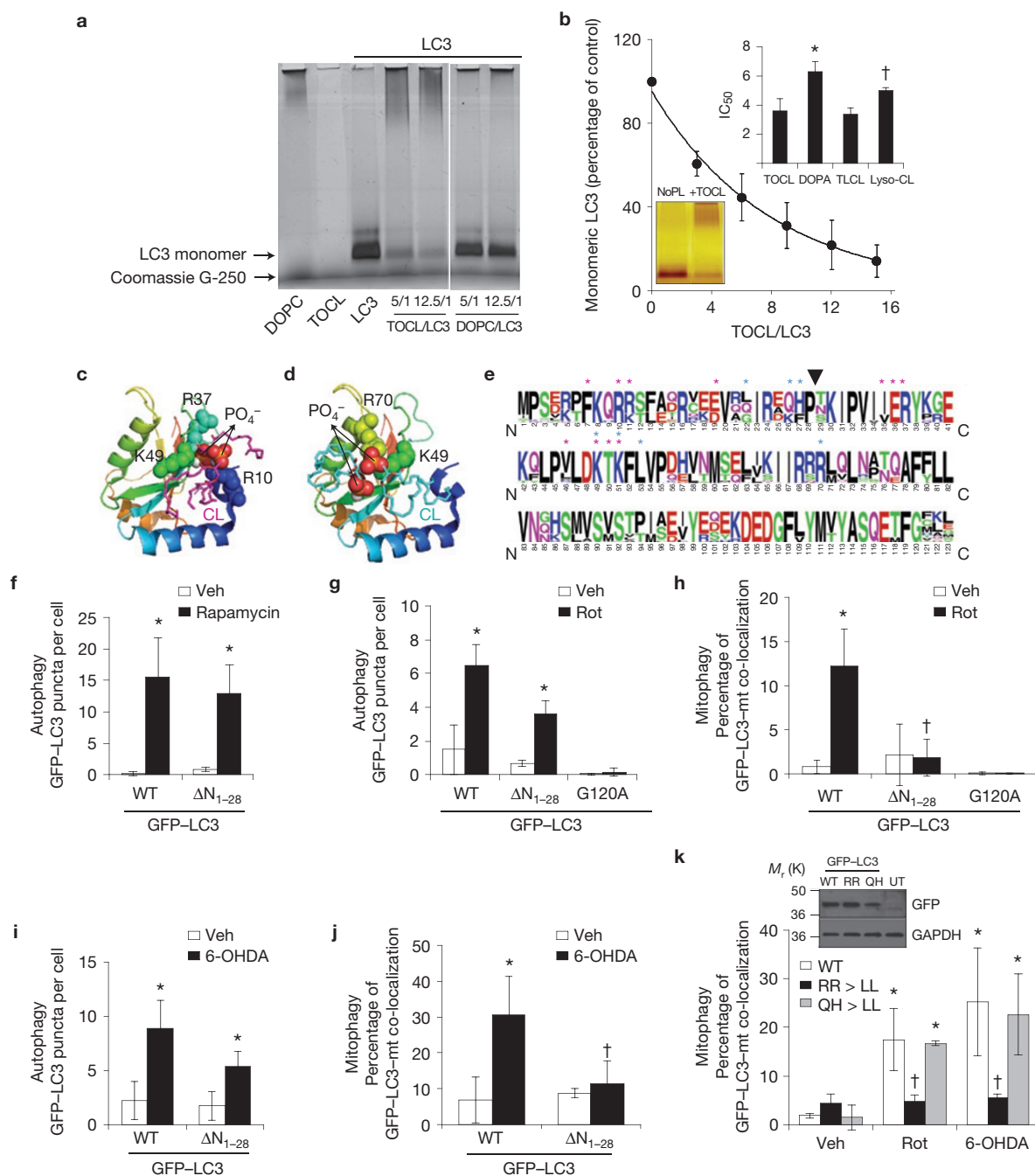
Figure 5 Mitochondrial recognition for mitophagy requires N-terminal amino acids of LC3. (a) Recombinant LC3 incubated with tetraoleoyl-CL (TOCL) or dioleoylphosphatidylcholine (DOPC) liposomes at the indicated molar ratios was analysed by blue native PAGE; liposome binding impaired the gel entry of proteins. (b) Titration of phospholipids (for example, TOCL) to LC3 was performed to evaluate the ratio that prevents 50% of the LC3 from entering the gels (IC_{50}) as an index of relative affinity. Bottom left inset: representative gel for TOCL/LC3 = 12; top right inset: comparison of IC_{50} values for TOCL versus dioleoyl-phosphatidic acid (DOPA) and tetralinoleoyl-CL (TLCL) versus monolyso-trilinoleoyl-CL (lyso-CL). The IC_{50} for DOPG was >15. *$P < 0.05$ versus TOCL; †$P < 0.05$ versus TLCL. (c,d) Molecular model of interaction sites for CL binding to LC3 by docking analysis. CL is coloured magenta in the top-ranked binding site conformation (c), and cyan in the alternative conformation (d), with the phosphates as spheres (oxygen, red; phosphorus, orange). Amino acids interacting with CL are represented as spheres along the LC3 ribbon structure, coloured blue > orange from N > C terminus. (e) Thirty-nine LC3 family sequences including isoforms A–C were aligned with ClustalW and displayed using WebLogo, with symbol heights corresponding to relative amino acid frequency. Asterisks denote residues predicted to contact CL in the favoured (magenta) and alternative conformations (cyan). (f–j) The arrowhead in e shows the position of the N-terminal truncation used to create GFP–LC3 deletion mutants, which were analysed for GFP–LC3 puncta formation (f,g,i) and participation in mitophagy (h,j) in response to the indicated stimuli. Rot, rotenone; Veh, vehicle. (e,k) Dual point mutations were prepared on the basis of predicted CL contact residues (e), and analysed for participation in mitophagy elicited by Rot or 6-OHDA (k). Inset: expression of GFP–LC3 plasmids (uncropped blots in Supplementary Fig. S7). UT, untransfected. Mean ± s.d. of $n = 3$ independent experiments for f–h, and $n = 4$ independent experiments for i,j (see Supplementary Table S4 for statistics source data); *$P < 0.05$ versus respective vehicle. †$P < 0.05$ versus toxin-treated wild type (WT).
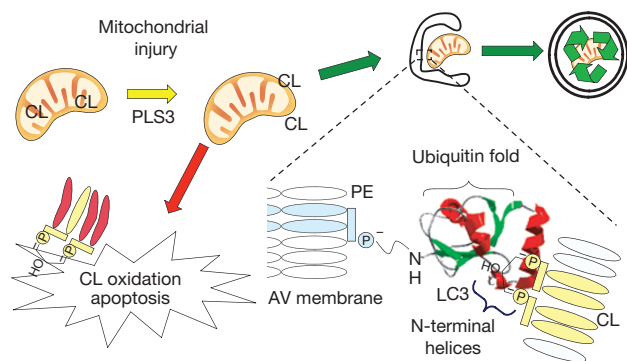
Figure 6 Schematic diagram summarizing the proposed role of CL in mitochondrial autophagy. Mitochondrial injuries induce a PLS3-dependent externalization of CL to the outer surface of mitochondria. Cargo incorporation into autophagosomes is facilitated by interactions of CL with the N-terminal domain of LC3. Clearance of CL-exposed mitochondria by mitophagy (green arrows) would be predicted to prevent CL oxidation and accumulation of pro-apoptotic signals (red arrow).

DISCUSSION

Taken together, the data presented in this study support a mechanism by which CL that is externalized in response to mitochondrial injury interacts with the autophagy protein LC3 to mediate targeted autophagy of mitochondria in primary neurons and transformed neuronal cells (Fig. 6). Interestingly, injured primary neurons exhibited greater fold increases in externalized mitochondrial CL when compared with CCCP-treated HeLa cells. These results suggest that different cell types may show different thresholds for engagement of particular mitophagy pathways, as supported by observations that primary neurons show diminished or delayed parkin translocation responses to CCCP (refs 33,34).

Although we cannot exclude the additional contribution of other anionic phospholipids, or of other mitochondrial–autophagosome adaptor proteins, studies of hypoxia-induced adaptors such as NIX and BNIP3 implicate additional signals or receptors for the incorporation of mitochondria into autophagosomes, as mitophagy was only partially blocked in their absence[35,36]. Here, we show several lines of evidence supporting an important role for CL–LC3 binding as a mitophagy signal. In addition to the strongest affinity exhibited by LC3 for CL relative to other phospholipids and the differences predicted by computational modelling, rotenone induced a disproportionate redistribution of CL relative to each of the other major mitochondrial phospholipids (compare Fig. 2a and Supplementary Fig. S2c). LC–MS analysis demonstrated a significantly lower content of PA than CL in the OMM after pro-mitophageal injury, and the PA that was present was not accessible to PLA_2-hydrolysis as an index of exposure to the surface, in agreement with published studies[37]. Moreover, two independent methods to downregulate OMM CL each suppressed mitochondrial delivery into the autophagolysosomal system. Reciprocally, site-directed mutagenesis of LC3 residues predicted to interact with CL by three computational approaches also suppressed mitophagy. This constellation of findings supports a key role for CL externalization in signalling the engulfment of mitochondria by the autophagic machinery.

Just as clustering or density of interactions is an important component of phosphatidylserine recognition for phagocytosis[38,39], we propose that a critical density of interactions may be needed to trigger mitophagy. Molecular modelling and simulations predict that clustering of CL around LC3 may serve to stabilize initial electrostatic interactions, with embedding of parts of the protein into the bilayer through hydrophobic interactions (Supplementary Fig. S6d,e). If this is correct, such a clustering mechanism could help ensure that normal transient fluctuations due to lipid transport dynamics do not trigger mitophagy until a critical threshold of LC3–CL interaction density is achieved. It is possible that in some model systems, the threshold may be modulated by concurrent engagement of other cargo-targeting mechanisms.

CL interacts with other mitochondrial proteins such as VDAC, which is also implicated in mitophagy[23,24]. Whether or not the effects of CL on VDAC gating functions[40] may potentially affect the role of VDAC in mitophagy, however, remains unknown. CL also plays a role in localizing IRGM to the inner membrane matrix fractions of macrophage mitochondria, allowing IRGM to regulate a cell fate switch between autophagic mycobacterial clearance and apoptosis[7]. Interestingly, the autophagy-promoting kinase AMPK is able to regulate CLS and nucleoside diphosphate kinase, another mitochondrial protein implicated in regulating the intermembrane distribution of CL (refs 41–43). Thus, it is possible that CL distribution is also important for mitophagy elicited downstream of AMPK pathways.

The endosymbiotic theory postulates that eukaryotic cells formed from symbiotic co-evolution with ingested bacteria-like organisms. The advantages of aerobic respiration created new cellular risks, however, as mitochondria are capable of generating ROS and releasing cell death mediators. It seems that yeast and mammals evolved distinct mechanisms to deal with this threat, as yeast proteins that mediate selective mitophagy have no mammalian orthologues[2]. Notably, the requirement for a specific spatial arrangement of amino acid residues for proteins that bind CL is different from the Ca^{2+} bridge employed for recognition of phosphatidylserine by phagocytosing cells[44], and the particular amino acids forming the CL-binding pocket of LC3 are highly conserved in vertebrates (Supplementary Table S3).

Owing to their metabolic features and post-mitotic state, neurons are particularly vulnerable to disrupted cellular quality control, and dysregulation of autophagy and cargo recognition are centrally implicated in Parkinson's disease, Alzheimer's disease, Huntington's disease and amyotrophic lateral sclerosis[10–12]. *PINK1* and *PARK2*, two genes mutated in recessive forms of familial parkinsonism, play important roles in the regulation of CCCP-induced mitophagy[3,24], and phosphorylation of a mitochondrial outer membrane protein regulates mitophagy during hypoxia[4]. Mitophagy functions as a pro-survival mechanism in PINK1-deficient cells[45]. Furthermore, CL interaction with IRGM is important for interferon-γ-induced mycobacterial clearance, although the effects were mediated through regulation of mitochondrial fission[7]. Nevertheless, as other bacteria are targeted intracellularly for autophagy through mechanisms that parallel recognition of protein aggregates[46], it is possible that CL may also serve as a molecular pattern recognition signal for xenophagy.

In summary, our data indicate that mammalian neurons have evolved mechanisms to trigger exposure of CL for recognition by the autophagy machinery, contributing another layer to cellular defences against the malfunctioning mitochondrial endosymbiont. Given that strong apoptotic stimuli result in caspase-mediated cleavage of beclin 1

(ref. 25), and oxidized CL is required for the release of pro-apoptotic factors into the cytosol, we further propose that, if the mitophagic machinery fails to eliminate damaged mitochondria, externalized CLs may then undergo oxidation as a prelude to apoptosis[47] (Fig. 6). □

METHODS

Methods and any associated references are available in the online version of the paper.

Note: Supplementary Information is available in the online version of the paper

AUTHOR CONTRIBUTIONS

J.J., R.K.D. and J.F.J. conducted and analysed experiments in the primary neuron, SH-SY5Y and HeLa cell systems, respectively. A.A.A., Y.Y.T. and V.A.T. collected and analysed the LC–MS data. K.Z.Q.W. contributed to LC3 mutagenesis and PLS3 knockdown studies. A.A.K performed the liposome studies. D.M., N.Y., J.K-S., I.H.S. and I.B. performed computational modelling. K.B., G.B. and Z.H. developed and optimized specific assays for the study. C.B. and S.W. performed specialized fluorescence microscopy. J.Z., A.M.G., E.K.S., R.W. and A.C. contributed to the PINK1, parkin, p62 and flux analyses. C.T.C., H.B. and V.E.K. planned and designed the study, analysed data, developed the conceptual model and wrote the manuscript. All authors discussed the results, and contributed to writing or commenting on the manuscript.

COMPETING FINANCIAL INTERESTS

The authors declare no competing financial interests.

Published online at www.nature.com/doifinder/10.1038/ncb2837
Reprints and permissions information is available online at www.nature.com/reprints

1. Kim, I. & Lemasters, J. J. Mitophagy selectively degrades individual damaged mitochondria after photoirradiation. *Antioxid. Redox Signal.* **14,** 1919–1928 (2011).
2. Kanki, T., Wang, K., Cao, Y., Baba, M. & Klionsky, D. J. Atg32 is a mitochondrial protein that confers selectivity during mitophagy. *Dev. Cell* **17,** 98–109 (2009).
3. Narendra, D., Tanaka, A., Suen, D. F. & Youle, R. J. Parkin is recruited selectively to impaired mitochondria and promotes their autophagy. *J. Cell Biol.* **183,** 795–803 (2008).
4. Liu, L. *et al.* Mitochondrial outer-membrane protein FUNDC1 mediates hypoxia-induced mitophagy in mammalian cells. *Nat. Cell Biol.* **14,** 177–185 (2012).
5. Schlame, M. Cardiolipin synthesis for the assembly of bacterial and mitochondrial membranes. *J. Lipid Res.* **49,** 1607–1620 (2008).
6. Beyer, K. & Nuscher, B. Specific cardiolipin binding interferes with labeling of sulfhydryl residues in the adenosine diphosphate/adenosine triphosphate carrier protein from beef heart mitochondria. *Biochemistry* **35,** 15784–15790 (1996).
7. Singh, S. B. *et al.* Human IRGM regulates autophagy and cell-autonomous immunity functions through mitochondria. *Nat. Cell Biol.* **12,** 1154–1165 (2010).
8. Sugawara, K. *et al.* The crystal structure of microtubule-associated protein light chain 3, a mammalian homologue of *Saccharomyces cerevisiae* Atg8. *Genes Cells* **9,** 611–618 (2004).
9. Miyanishi, M. *et al.* Identification of Tim4 as a phosphatidylserine receptor. *Nature* **450,** 435–439 (2007).
10. Schon, E. A. & Przedborski, S. Mitochondria: the next (neurode)generation. *Neuron* **70,** 1033–1053 (2011).
11. Zhu, J. H., Guo, F., Shelburne, J., Watkins, S. & Chu, C. T. Localization of phosphorylated ERK/MAP kinases to mitochondria and autophagosomes in Lewy body diseases. *Brain Pathol.* **13,** 473–481 (2003).
12. Wong, E. & Cuervo, A. M. Autophagy gone awry in neurodegenerative diseases. *Nat. Neurosci.* **13,** 805–811 (2010).
13. Barth, S., Glick, D. & Macleod, K. F. Autophagy: assays and artifacts. *J. Pathol.* **221,** 117–124 (2010).
14. Tyurin, V. A. *et al.* Oxidative lipidomics of programmed cell death. *Methods Enzymol.* **442,** 375–393 (2008).
15. Crompton, M., Barksby, E., Johnson, N. & Capano, M. Mitochondrial intermembrane junctional complexes and their involvement in cell death. *Biochimie* **84,** 143–152 (2002).
16. Andree, H. A. *et al.* Binding of vascular anticoagulant alpha (VAC alpha) to planar phospholipid bilayers. *J. Biol. Chem.* **265,** 4923–4928 (1990).
17. Dagda, R. K., Zhu, J., Kulich, S. M. & Chu, C. T. Mitochondrially localized ERK2 regulates mitophagy and autophagic cell stress: implications for Parkinson's disease. *Autophagy* **4,** 770–782 (2008).
18. Chalovich, E. M., Zhu, J. H., Caltagarone, J., Bowser, R. & Chu, C. T. Functional repression of cAMP response element in 6-hydroxydopamine-treated neuronal cells. *J. Biol. Chem.* **281,** 17870–17881 (2006).
19. Liu, J. *et al.* Role of phospholipid scramblase 3 in the regulation of tumor necrosis factor-alpha-induced apoptosis. *Biochemistry* **47,** 4518–4529 (2008).
20. Huang, Z. *et al.* Cardiolipin deficiency leads to decreased cardiolipin peroxidation and increased resistance of cells to apoptosis. *Free Radic. Biol. Med.* **44,** 1935–1944 (2008).
21. Ji, J. *et al.* Lipidomics identifies cardiolipin oxidation as a mitochondrial target for redox therapy of brain injury. *Nat. Neurosci.* **15,** 1407–1413 (2012).
22. Huang, W. *et al.* Crystal structure and biochemical analyses reveal Beclin 1 as a novel membrane binding protein. *Cell Res.* **22,** 473–489 (2012).
23. Sun, Y., Vashisht, A. A., Tchieu, J., Wohlschlegel, J. A. & Dreier, L. Voltage-dependent Anion Channels (VDACs) Recruit Parkin to defective mitochondria to promote mitochondrial autophagy. *J. Biol. Chem.* **287,** 40652–40660 (2012).
24. Geisler, S. *et al.* PINK1/Parkin-mediated mitophagy is dependent on VDAC1 and p62/SQSTM1. *Nat. Cell Biol.* **12,** 119–131 (2010).
25. Wirawan, E. *et al.* Caspase-mediated cleavage of Beclin-1 inactivates Beclin-1-induced autophagy and enhances apoptosis by promoting the release of proapoptotic factors from mitochondria. *Cell Death Dis.* **1,** e18 (2010).
26. Matsuda, N. *et al.* PINK1 stabilized by mitochondrial depolarization recruits Parkin to damaged mitochondria and activates latent Parkin for mitophagy. *J. Cell Biol.* **189,** 211–221 (2010).
27. Vives-Bauza, C. *et al.* PINK1-dependent recruitment of Parkin to mitochondria in mitophagy. *Proc. Natl Acad. Sci. USA* **107,** 378–383 (2010).
28. Narendra, D. P. *et al.* PINK1 is selectively stabilized on impaired mitochondria to activate Parkin. *PLoS Biol.* **8,** e1000298 (2010).
29. Kondapalli, C. *et al.* PINK1 is activated by mitochondrial membrane potential depolarization and stimulates Parkin E3 ligase activity by phosphorylating Serine 65. *Open Biol.* **2,** 120080 (2012).
30. Okatsu, K. *et al.* p62/SQSTM1 cooperates with Parkin for perinuclear clustering of depolarized mitochondria. *Genes Cells* **15,** 887–900 (2010).
31. Johansen, T. & Lamark, T. Selective autophagy mediated by autophagic adapter proteins. *Autophagy* **7,** 279–296 (2011).
32. Shvets, E., Fass, E., Scherz-Shouval, R. & Elazar, Z. The N-terminus and Phe52 residue of LC3 recruit p62/SQSTM1 into autophagosomes. *J. Cell Sci.* **121,** 2685–2695 (2008).
33. Van Laar, V. S. *et al.* Bioenergetics of neurons inhibit the translocation response of Parkin following rapid mitochondrial depolarization. *Human Mol. Genet.* **20,** 927–940 (2011).
34. Cai, Q., Zakaria, H. M., Simone, A. & Sheng, Z. H. Spatial parkin translocation and degradation of damaged mitochondria via mitophagy in live cortical neurons. *Curr. Biol.* **22,** 545–552 (2012).
35. Novak, I. *et al.* Nix is a selective autophagy receptor for mitochondrial clearance. *EMBO Rep.* **11,** 45–51 (2010).
36. Hanna, R. A. *et al.* Microtubule-associated protein 1 light chain 3 (LC3) interacts with Bnip3 protein to selectively remove endoplasmic reticulum and mitochondria via autophagy. *J. Biol. Chem.* **287,** 19094–19104 (2012).
37. Connerth, M. *et al.* Intramitochondrial transport of phosphatidic acid in yeast by a lipid transfer protein. *Science* **338,** 815–818 (2012).
38. Borisenko, G. G. *et al.* Macrophage recognition of externalized phosphatidylserine and phagocytosis of apoptotic Jurkat cells–existence of a threshold. *Arch. Biochem. Biophys.* **413,** 41–52 (2003).
39. Ravichandran, K. S. Find-me and eat-me signals in apoptotic cell clearance: progress and conundrums. *J. Exp. Med.* **207,** 1807–1817 (2010).
40. Rostovtseva, T. K., Kazemi, N., Weinrich, M. & Bezrukov, S. M. Voltage gating of VDAC is regulated by nonlamellar lipids of mitochondrial membranes. *J. Biol. Chem.* **281,** 37496–37506 (2006).
41. Athea, Y. *et al.* AMP-activated protein kinase alpha2 deficiency affects cardiac cardiolipin homeostasis and mitochondrial function. *Diabetes* **56,** 786–794 (2007).
42. Onyenwoke, R. U. *et al.* AMPK directly inhibits NDPK through a phosphoserine switch to maintain cellular homeostasis. *Mol. Biol. Cell* **23,** 381–389 (2012).
43. Schlattner, U. *et al.* Dual function of mitochondrial Nm23-H4 in phosphotransfer and intermembrane lipid transfer: a cardiolipin-dependent switch. *J. Biol. Chem.* **288,** 111–121 (2013).
44. Verdaguer, N., Corbalan-Garcia, S., Ochoa, W. F., Fita, I. & Gomez-Fernandez, J. C. Ca(2+) bridges the C2 membrane-binding domain of protein kinase Calpha directly to phosphatidylserine. *EMBO J.* **18,** 6329–6338 (1999).
45. Dagda, R. K. *et al.* Loss of pink1 function promotes mitophagy through effects on oxidative stress and mitochondrial fission. *J. Biol. Chem.* **284,** 13843–13855 (2009).
46. Wild, P. *et al.* Phosphorylation of the autophagy receptor optineurin restricts Salmonella growth. *Science* **333,** 228–233 (2011).
47. Kagan, V. E. *et al.* Cytochrome c acts as a cardiolipin oxygenase required for release of proapoptotic factors. *Nat. Chem. Biol.* **1,** 223–232 (2005).

METHODS

Primary cortical neuron cultures were prepared from E16 Sprague–Dawley rats (Charles River Laboratory), employing 0.25% trypsin with EDTA (Invitrogen) for 15–20 min at 37 °C, followed by trituration in ice-cold Neurobasal medium and plating in poly-D-lysine coated plates, following protocols approved by the University of Pittsburgh Institutional Animal Care and Use Committee. Experiments were performed at 7–9 days *in vitro* (>95% neurons, <5% astroglia), employing sublethal conditions[48] (Supplementary Fig. S1a) for rotenone (125 nM–250 nM × 2 h), STS (100 nM × 2 h) or dimethylsulphoxide (DMSO; Sigma) as vehicle control.

SH-SY5Y, a human neuroblastoma cell line (ATCC) that expresses tyrosine hydroxylase and dopamine transporter, was maintained in antibiotic-free Dulbecco's modified Eagle's medium (BioWhittaker; supplemented with 10% fetal bovine serum (Gibco/Invitrogen), 15 mM HEPES and 2 mM glutamine, with 5% CO_2 at 37 °C. All cells were verified as mycoplasma-free using Lonza's MycoAlert mycoplasma detection kit. Cells are routinely tested every one to two months. To stimulate mitophagy, SH-SY5Y cells were treated with rotenone (1 μM), STS (1 μM), 6-hydroxydopamine (120 μM), FCCP (2–5 μM), rapamycin (50 μM) or vehicle for 4 h. HeLa cells (ATCC) expressing parkin (Germantown) were cultured in DMEM supplemented with 10% FBS. For mitophagy induction, cells were treated with 20 μM CCCP for 4 h.

RNAi sequences and antibodies. The following RNAi sequences were used: CLS siRNA (rat, 5′-CGCGAACACUAGCUAAGUAtt-3′, 5′-GGAUUUGUUGGAUGGA-UUUtt-3′, 5′-CCCACUCACUUACAUGAUAtt-3′, pooled, S172628, S172627, S172626, Life Technologies); CLS siRNA2 (rat, 5′-GGAUGGAUUUAUUGCUCG-Att-3′, J-093152-09-0002, Thermo Fischer Scientific); CLS siRNA (human, 5′-GCUUAUAGUUACUAUCAUUTT-3′, S29308, Ambion, Life Technologies); PLS3 siRNA 433 and 508 (human, 5′-GCCTCGAATTCCTGGTG CAGA-3′ and 5′-GGGAGACCTGTAATCGGTATGAACT-3′, Stealth RNAi Pre-Designed siRNAs, Invitrogen); LC3B siRNA (human, 5′-GAAGGCGCUUACAGCUCAA-3′); and ATG7 siRNA (human, 5′-GCCAGUGGGUUUGGAUCAA-3′) as previously described[17].

The antibodies used were as follows: rabbit-anti-LC3 (1:1,000, #2775, Cell Signaling); mouse-anti-LC3 (1:200, LC3-5F10: 0231-100, Nanotools); mouse-anti-TOM40 (1:1,000, D-2: SC-365467), rabbit anti-TOM40 (1:1,000, H-300: SC-11414), goat anti-LDH-A (1:1,000, V-17: SC-27232), and rabbit anti-GAPDH (1:1,000, SC-25778) from Santa Cruz Biotechnology; rabbit-anti-MnSOD (1:1,000, DD-17: S5069), mouse-anti-actin (1:2,000, clone AC-40: A3853) and rabbit-anti-actin (1:2,000, A2066 (C11 peptide) or A5441) from Sigma; mouse anti-MnSOD (1:1,000, clone 19: 611580, BD Pharmingen); mouse anti-human mito. antigen p60 (1:1,000, MU213-UC, Biogenex); mouse anti-p62 (1:1,000 (western blotting), 1:200 (immunocytochemistry), 610832, BD Biosciences); and rabbit anti-GFP (1:5,000, A6455, Invitrogen). We thank P. J. Sims, University of Rochester School of Medicine, USA, for the mouse anti-human scramblase-3 (1:500).

Transfections and image analysis. Cortical neurons and SH-SY5Y cells were transfected using Lipofectamine 2000 (Invitrogen) as previously described. Plasmids included mtDsRed2 (Clontech), Mito-GFP (Clontech), GFP-tagged or RFP-tagged LC3 (T. Yoshimori, Research Institute of Microbial Diseases, Osaka University, Japan), mCherry-tagged p62/SQSTM1 (Z. Yue, Mount Sinai, New York, USA) or untagged mouse phospholipid scramblase 3 in pcMV6-XL4 (Origene). Primary neurons were transfected at 4 days *in vitro* with 45 nmol of small interfering RNA (siRNA), using Lipofectamine 2000 (Life Technologies). For HeLa cells, siRNA targeting human CLS or negative control siRNAs were transfected using RNAiMax (Life Technologies) and two distinct siRNAs targeting human PLS3 sequences beginning at nucleotide 433 or 508 (Invitrogen), siRNA targeting human LC3B (ATG8; ref. 17), human ATG7 (ref. 17) and/or scrambled siRNA non-targeting controls (Life Technologies) were used for SH-SY5Y cells. All STS, rotenone, 6-OHDA, FCCP, CCCP or vehicle treatments were performed 72 h following plasmid or siRNA transfection.

Fluorescence images were captured as *z*-stacks (0.5 μm slices, 640×640 pixel resolution, 20 μs per pixel) encompassing the depth of the cell using an Olympus Fluoview 1000 confocal microscope (×60 oil immersion lens, NA 1.42), using sequential laser imaging and Kalman filter correction. Coverslips/wells were imaged randomly, scanning for 3–5 fields in each quadrant; 20–30 neurons per coverslip or 15–55 transfected cells were imaged per experiment. Images were coded, and total numbers and numbers of co-localizing LC3 puncta were analysed by an individual blinded to the condition. Numbers of fluorescent LC3 puncta elicited per cell, western blot analysis of LC3-II, and mitophagy analysis by co-localization of mitochondria with early and late autophagolysosomal markers were performed as described previously[45,49].

Completion of mitophagy was analysed by immunoblot for levels of outer mitochondrial membrane (OMM), inner mitochondrial membrane (IMM) and matrix proteins. Bafilomycin (50 nM × 1 h) was used in some experiments to arrest autophagosome degradation.

Biochemical studies. Mitochondria were prepared using a combination of differential and Percoll gradient centrifugation (Sims and Anderson, 2008). The IMM and OMM fractions were obtained as previously described[33]. Samples were centrifuged (12,000*g*) and the pellets and supernatants collected as IMM and OMM fractions, respectively. The purity of fractions was verified by two methods, immunoblot analysis of COX4, TOM40, ANT or VDAC, and by quantitative LC–MS analysis of characteristic phospholipid distribution.

Cell lysates or fractions from isolated mitochondria were washed with PBS, lysed in 0.1% Triton X-100 with protease/phosphatase inhibitor cocktail, and protein concentration was determined by Coomassie Plus Protein Assay (Pierce). Loading was adjusted for relative protein yields of different subcellular fractions to enable comparisons of equivalent cell numbers. Standard immunoblot procedures were employed.

Quantitative mass spectrometry. Individual phospholipid classes from mitochondrial inner and outer membranes were resolved using normal-phase silica column chromatography (Luna, 3 μm, 15 cm × 2 mm i.d. Phenomenex), coupled to a Shimadzu Prominence HPLC system (Shimadzu), with elution at 0.2 ml min^{-1} employing a linear gradient (Solvent A: chloroform/methanol/triethylamine/acetic acid (80:19:0.5:0.5); Solvent B: chloroform/methanol/water/triethylamine/acetic acid (60:33.5:5.5:1.0:0.065)). Phospholipids were analysed on a Waters quadrupole time-of-flight mass spectrometer (Waters) using the following parameters: capillary voltage, 2.85 kV, negative mode; source temperature, 100 °C; desolvation gas, 400 L h^{-1}; sampling cone, 60 V; extraction cone: 4.5 V; ion guide, 3.0 V. Tuning was optimized for all lipids across the scan range. For some samples, an ion trap platform was also used for analysis. For quantitative analysis of CL, samples were mixed with an internal standard (1, 1′, 2, 2′-tetramyristoyl-CL, Avanti Polar Lipids). Nanomoles of individual molecular species of CL were calculated by determining the ratio of the peak area of the CL molecular species of interest to the internal standard. In addition to TMCL, the following phospholipid internal standards were used with fatty acid chains as follows: phosphatidylglycerol (12:0/12:0); phosphatidylinositol (16:0/16:0); phosphatidic acid (17:0/17:0); phosphatidylethaolamine (17:0/17:0); phosphatidylserine (17:0/17:0); phosphatidylcholine (11:0/11:0); and sphingomyelin (18:1/18:0). The CL content was normalized as picomoles of CL per nanomole of total mitochondrial phospholipid phosphorus or as nanomoles of CL per milligram of mitochondrial protein.

CL exposure on the outer surface of mitochondria. To quantify the content of CL exposed to the outside of mitochondria, we treated intact mitochondria with 0.7 U mg^{-1} protein of an anionic phospholipid-selective PLA$_2$ (Porcine pancreatic, Sigma)[50], in the presence of fatty-acid-free human serum albumin (20 mg ml^{-1}, 4 °C, 50 min) to prevent membrane damage by CL hydrolysis products such as lyso-CLs and free fatty acids[51]. Normal-phase LC–MS was employed to detect lyso-hydrolysis products before and after cleavage with PLA$_2$, as described above.

Annexin V binds anionic phospholipids in a calcium-dependent manner. It has the highest affinity for CL based on the [Ca^{2+}] required for half-maximal binding, as the unique phospholipid head group of CL is more effective at charge clustering[16,17]. To validate and optimize the annexin V binding assay for externalized CL, isolated liver mitochondria[52] were coated with different phospholipids (50 pmol mg^{-1} protein) and annexin V binding was assessed by flow cytometry in the presence of increasing [Ca^{2+}] (Supplementary Fig. S2d). The assay was further validated using cells depleted of phospholipid scramblase 3, an enzyme that mediates CL redistribution to the OMM.

To measure the extent of CL externalization in response to mitophagy-inducing treatments, cells seeded on 100 mm tissue culture plates were pre-transfected with Mito-GFP or stained with 250 nM MitoTracker Green FM (Invitrogen) for 45 min at 37 °C to label mitochondria. In some experiments, SH-SY5Y cells were first transfected with control siRNA or PLS3 siRNA using Lipofectamine 2000 (ref. 17), and treated 3 days later. Each independent experiment involved pooling cells from five plates per condition for mitochondrial isolation. Isolated mitochondria were incubated with Alexa 647-labelled annexin V (Invitrogen) in buffer maintained at 15 nmol Ca^{2+} μg^{-1} protein to stain surface-exposed anionic phospholipids and then subjected to flow cytometric analysis (FACSCanto, Becton-Dickinson) of red fluorescence (excitation/emission, 633/660 nm) employing appropriate settings for forward light scatter and side light scatter detectors. The Alexa fluorescence from gated green fluorescent mitochondria events (excitation/emission, 488/530 nm) was used to evaluate the binding of annexin-V to mitochondria.

Molecular modelling and sequence alignment. Marvin Sketch (v. 5.3.6, 2010) was used for displaying chemical structures and generating three-dimensional structures corresponding to the lowest energy conformer (http://www.chemaxon.

com). CL was docked to the crystal structure of LC3 (PDBid:1UGM; ref. 8) using AutoDock Vina[53] (http://vina.scripps.edu). Lipid and protein structures were converted from pdb into pdbqt format using MGL Tools[54]. LC3 was treated as the receptor and kept rigid during docking, maintaining flexibility of rotatable bonds in CL. A grid box was centred at the −11.358, 37.55, 13.575 coordinates with 40 Å units in x, y and z directions to cover the entire LC3 protein. AutoDock Vina reports the 9 lowest energy conformations, which were inspected using PyMOL software (www.pymol.org). All computational calculations (docking and molecular dynamics) have been done using the published LC3B structure[8] (1UGM).

A total of 39 sequences corresponding to the LC3 family corresponding to isoforms (A–C) were downloaded from SwissProt[55] using the criteria (*(gene:MAP1LC3B OR gene:MAP1LC3A OR gene:MAP1LC3C)) AND fragment:no*, aligned with ClustalW[56] and displayed using WebLogo[57].

See Supplementary Note for methods pertaining to the full atomic and coarse-grained molecular dynamics simulations of Supplementary Fig. S6.

Preparation of liposomes. The following were obtained from Avanti Polar Lipids: 1,2-dioleoyl-*sn*-glycero-3-phosphocholine (DOPC), 1,1′,2,2′-tetraoleoyl-CL (TOCL), 1,1′,2,2′-tetralinoleoyl-CL (TLCL), monolyso-tri-linoleoyl-CL (lyso-CL), 1,2-dioleoyl-*sn*-glycero-3-phosphate (DOPA) and 1,2-dioleoyl-*sn*-glycero-3-phospho-(1′-*rac*-glycerol) (DOPG). Phospholipids, stored in chloroform, were mixed and dried under nitrogen, then mixed in a vortex in HEPES buffer (20 mM, pH 7.4) and sonicated 3× for 30 s on ice. Liposomes were used immediately after preparation.

Phospholipid–LC3 native blue gel shift binding assay. Recombinant human His6–LC3/MAP1LC3A (R&D Systems) (4 µM) was incubated in 25 mM HEPES buffer (pH 7.4) with liposomes containing different ratios of TOCL, DOPA, DOPI or DOPG, on a DOPC backbone for 10 min at room temperature, followed by native blue electrophoresis in 4–16% bis–tris gels, and silver staining using GelCode SilverSNAP kit (Fisher Scientific). In some experiments, recombinant rat LC3B (gift from Y. Uchiyama, Juntendo University Graduate School of Medicine, Tokyo, Japan) was used. Densitometric analysis of gels was performed and the percentage of monomeric LC3 in the gel was determined. Lipid/LC3 ratios preventing 50% of the LC3 monomer from entering the gel were determined from analysis of the plots of percentage monomeric LC3 versus lipid/LC3 ratio for each individual phospholipid. TLCL and lyso-CL were also employed to investigate the possible role of acyl chain numbers.

Custom-synthesized (LifeTein LLC) N-terminal human LC3A wild-type and mutant ($R_{10}R_{11} > L_{10}L_{11}$) peptides (amino acid sequences 1–30; 1.5 µM) were incubated in 25 mM HEPES buffer (pH 7.4) with liposomes containing TOCL/DOPC at a TOCL/LC3 ratio of 6 (10 min at room temperature). This was followed by native blue electrophoresis in 4–16% bis–tris gel, and silver staining using the GelCode SilverSNAP kit (Fisher Scientific).

Mutagenesis. An N-terminal deletion mutant plasmid for GFP–LC3 ($\Delta 1$–28) was generated by PCR using forward and reverse primers that harbour a BglII restriction site and an EcoRI restriction site, respectively, and the complementary DNA for the first β-sheet of rat LC3 (5′-TATAGAATTCTATGAACCAAGATCCCAGTGATTAT-3′). The purified DNA fragment was subjected to enzymatic digestion with BglII and EcoRI restriction enzymes and ligated onto BglII and EcoRI pre-digested pEGFP-C1 vector backbone. The GFP–LC3(R10L,R11L) (forward primer: 5′-GAG AAGACCTTCAAACAG CTCCTGAGCTTCGAACAAAGAGTG-3′, reverse primer: 5′-CACTCTTTGTTCGAAGCTCAGGAGCTGTTTGAAGGTCTTCTC-3′) and GFP–LC3(Q26L,H27L) (forward primer: 5′-CGGCTCATCCGGGAGCTGCTTCC-CACCAAGATCCCAG-3′, reverse primer: 5′-CTGGGATCTTGGTGGGAAGCA GCTCCCGG ATGAGCCG-3′) mutant plasmids were generated by QuickChange II XL site-directed mutagenesis kit (Agilent Technologies) according to the manufacturer's instructions. The cDNA sequences in all mutant constructs were confirmed by DNA sequencing analysis. The expression levels of the recombinant constructs were evaluated in transfected SH-SY5Y cells by immunoblotting with anti-GFP antibody (Fig. 5k inset). The GFP–LC3 mutant containing a C-terminal glycine to alanine mutation (G120A) that is impaired for binding to autophagosomes was obtained from T. Yoshimori (Graduate School of Biosciences and Frontier Bioscience, Osaka University, Suita-Osaka, Japan).

Statistics. For fluorescence experiments, all in-focus cells, expressing the appropriate transfection marker if applicable, from 12–15 randomly captured fields per slide were analysed. The average value per cell was determined for each independent experiment. The results from each independent experiment were then averaged and expressed as the mean of $n = 3$–7 independent experiments, ±standard deviation (s.d.). The data were analysed by one-way analysis of variance for multi-group parametric comparisons or two-tailed t-tests for parametric comparisons involving two samples. For western blot quantification, densitometry was performed and the normalized values from independent experiments were averaged. Significance was set at $P < 0.05$.

48. Tyurin, V. A. *et al*. Mass-spectrometric characterization of phospholipids and their primary peroxidation products in rat cortical neurons during staurosporine-induced apoptosis. *J. Neurochem*. **107**, 1614–1633 (2008).
49. Zhu, J., Dagda, R. K. & Chu, C. T. Monitoring mitophagy in neuronal cell cultures. *Methods Mol. Biol*. **793**, 325–339 (2011).
50. Yu, B. Z. *et al*. Structural basis of the anionic interface preference and kcat* activation of pancreatic phospholipase A2. *Biochemistry* **39**, 12312–12323 (2000).
51. Nilsson, O. S. & Dallner, G. Transverse asymmetry of phospholipids in subcellular membranes of rat liver. *Biochim. Biophys. Acta* **464**, 453–458 (1977).
52. Frezza, C., Cipolat, S. & Scorrano, L. Organelle isolation: functional mitochondria from mouse liver, muscle and cultured fibroblasts. *Nat. Protoc*. **2**, 287–295 (2007).
53. Trott, O. & Olson, A. J. AutoDock Vina: improving the speed and accuracy of docking with a new scoring function, efficient optimization, and multithreading. *J. Comput. Chem*. **31**, 455–461 (2010).
54. Sanner, M. F. Python: a programming language for software integration and development. *J. Mol. Graph. Model*. **17**, 57–61 (1999).
55. Boeckmann, B. *et al*. The SWISS-PROT protein knowledgebase and its supplement TrEMBL in 2003. *Nucleic Acids Res*. **31**, 365–370 (2003).
56. Thompson, J. D., Gibson, T. J. & Higgins, D. G. Multiple sequence alignment using ClustalW and ClustalX. *Curr. Protoc. Bioinformatics* 2.3.1–2.3.22.
57. Crooks, G. E., Hon, G. & Chandonia, J. M. WebLogo: a sequence logo generator. *Genome Res*. **14**, 1188–1190 (2004).
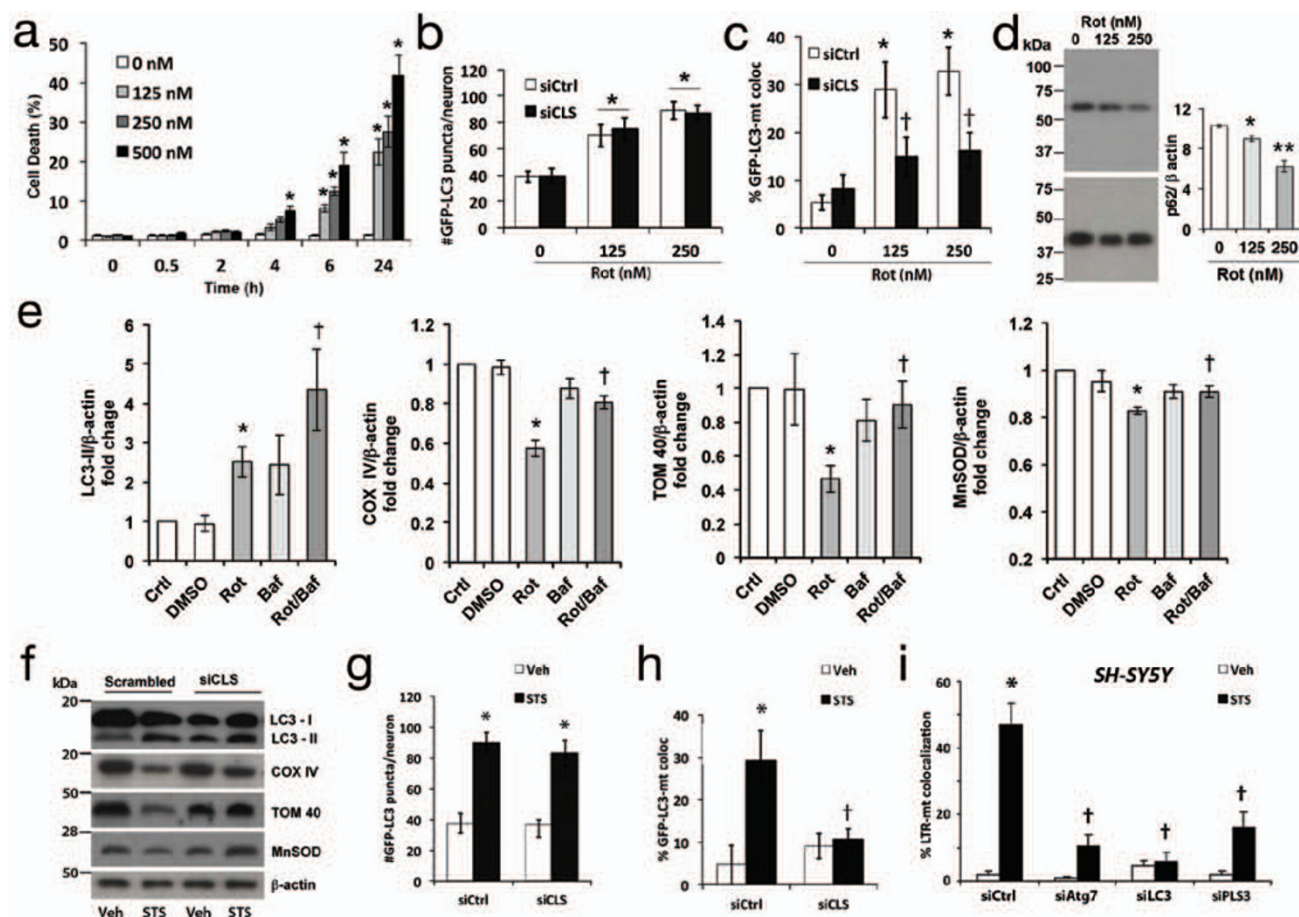
Figure S1 Additional characterization of Rot and STS-induced mitophagy. Primary rat cortical neuron cultures were treated with rotenone at 7-9 days *in vitro* (DIV) using the indicated doses and times. Cell death was analyzed by flow cytometry of Annexin V/propidium iodide stained neurons to define sub-lethal conditions (a). N=6 independent experiments; mean +/- s.d., *p < 0.05 vs. vehicle. Equivalent results were observed for caspase-3/7 activation (not shown), assayed using the luminescent Promega Caspase-Glo assay (Madison, WI). Rotenone elicited increased GFP-LC3 puncta (b) and colocalization with mitochondria (c), the latter of which was inhibited by siRNA knockdown of CLS (siCLS), but not scrambled siCtrl. For b,c: N=3; mean +/- s.d. * p<0.05 vs. vehicle-treated neurons; † p<0.05 vs. respective Rot-treated siCtrl neurons. Primary cortical neurons treated with vehicle or the indicated concentrations of rotenone were analyzed for p62 protein levels by immunoblot. Densitometry indicates significant decreases in p62 levels,

consistent with dose-dependent increases in autophagic flux (d). N=3; mean +/- s.d. *p<0.01 vs. vehicle; **p<0.01 vs. Rot 125 nM. Densitometry of mitochondrial proteins analyzed by immunoblot (See Fig. 1g) confirmed decreased protein levels, inhibited by co-treatment with bafilomycin (e). N=3; mean +/- s.d., *p<0.05 vs. Ctrl; †p<0.05 vs. Rot alone. Primary neurons transfected on DIV 4 with siCLS or siCtrl were treated with STS on DIV 7 and analyzed for autophagy by LC3 shift (f) and GFP-LC3 puncta (g), and for mitophagy by colocalization analysis (h) or by loss of mitochondrial proteins (f). For g,h: N=3; mean +/- s.d *p<0.05 vs. respective vehicle-treated neurons; †p<0.05 vs. STS-treated siCtrl neurons. STS also elicited mitophagy in SH-SY5Y cells (i), as assessed by delivery of mitochondria to LTR-labeled lysosomes, which was inhibited by siRNA knockdown of the autophagy proteins Atg7 or LC3, as well as PLS3. * p<0.05 vs Veh; † p<0.05 vs STS/siCtrl.
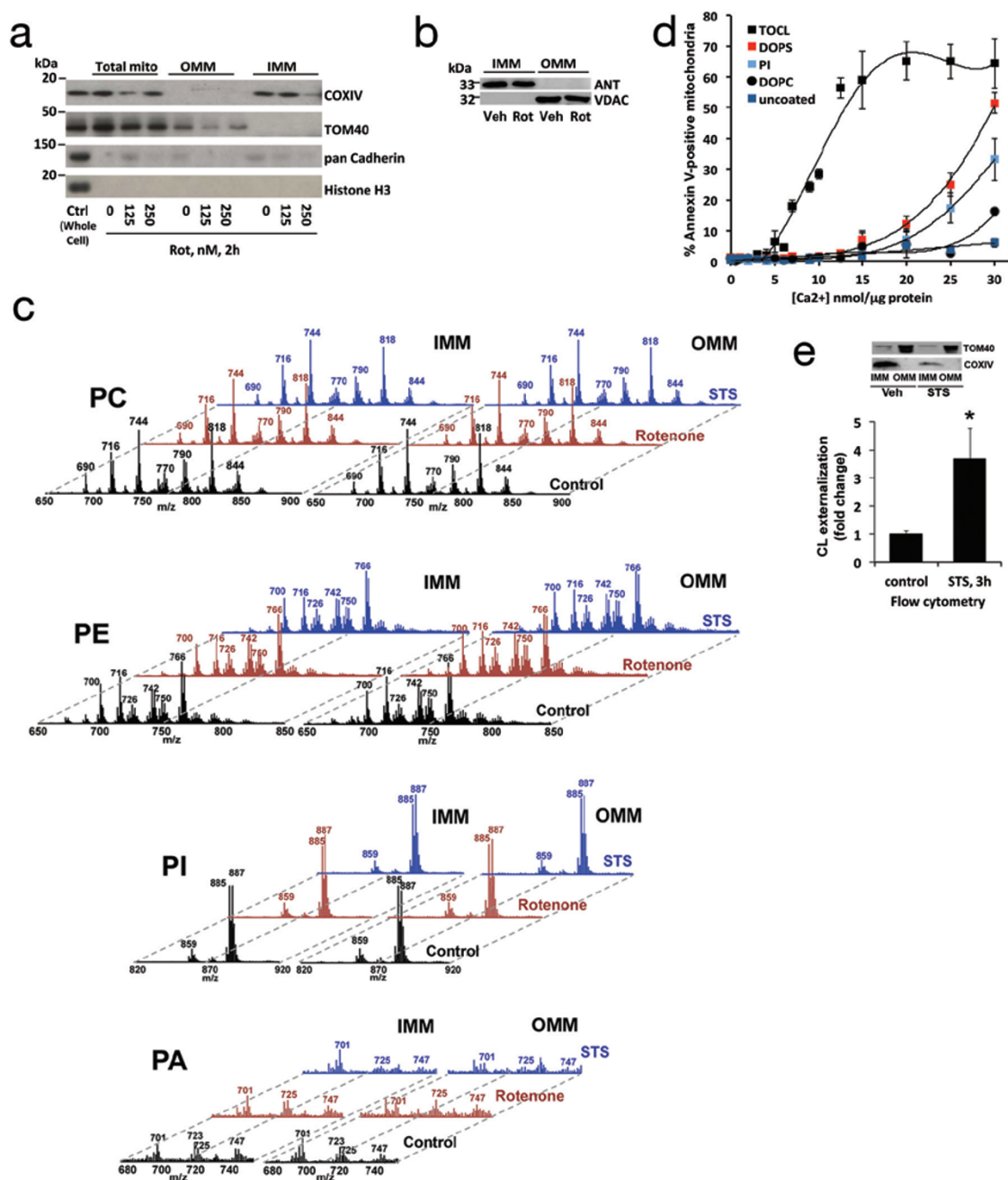
Figure S2 Mitochondrial isolation and characterization of phospholipid content and accessibility. Primary cortical neuron cultures (DIV 7 or 8) were exposed to rotenone followed by isolation of mitochondrial IMM and OMM for LC-MS analysis. Immunoblot analysis employed the following (a): COXIV - IMM marker; TOM40 - OMM marker; pan Cadherin - cellular membrane marker; Histone H3 - nuclear marker. Western blot analysis for contact site IMM and OMM proteins ANT and VDAC, respectively, revealed no significant cross-contamination of fractions (b, Rot, 250 nM x 2h, representative of 3 experiments). Neuronal cells were treated with rotenone (250 nM) or STS (100 nM), and the IMM and OMM fractions prepared from isolated mitochondria were pooled from 3 experiments for lipid extraction and LC-MS analysis as described in Methods. Representative spectra for phosphatidylcholine (PC), phosphatidylethanolamine (PE), phosphatidylinositol (PI), and phosphatidic acid (PA) are shown for mitochondrial membranes isolated from control, rotenone- and STS-treated neurons (c). In contrast to CL (Fig. 2a), only subtle changes in peak distribution, intensity, or cluster pattern of IMM and OMM PC, PE, PI and PA were observed. Isolated liver mitochondria labeled with the indicated phospholipids were mixed with Annexin V in the presence of the indicated Ca^{2+} concentrations. Annexin V binding was assessed by flow cytometry, indicating specificity for CL at lower Ca^{2+} concentrations (d). The highest concentration shown is equivalent to 300 μM. N=4 experiments, mean +/- s.d. STS-treated HeLa cells exhibited increased surface accessibility of CL on isolated mitochondria probed with Annexin V (e). Inset: purity of membrane fractions. * p<0.05 vs. control. N=3 experiments, mean +/- s.d.
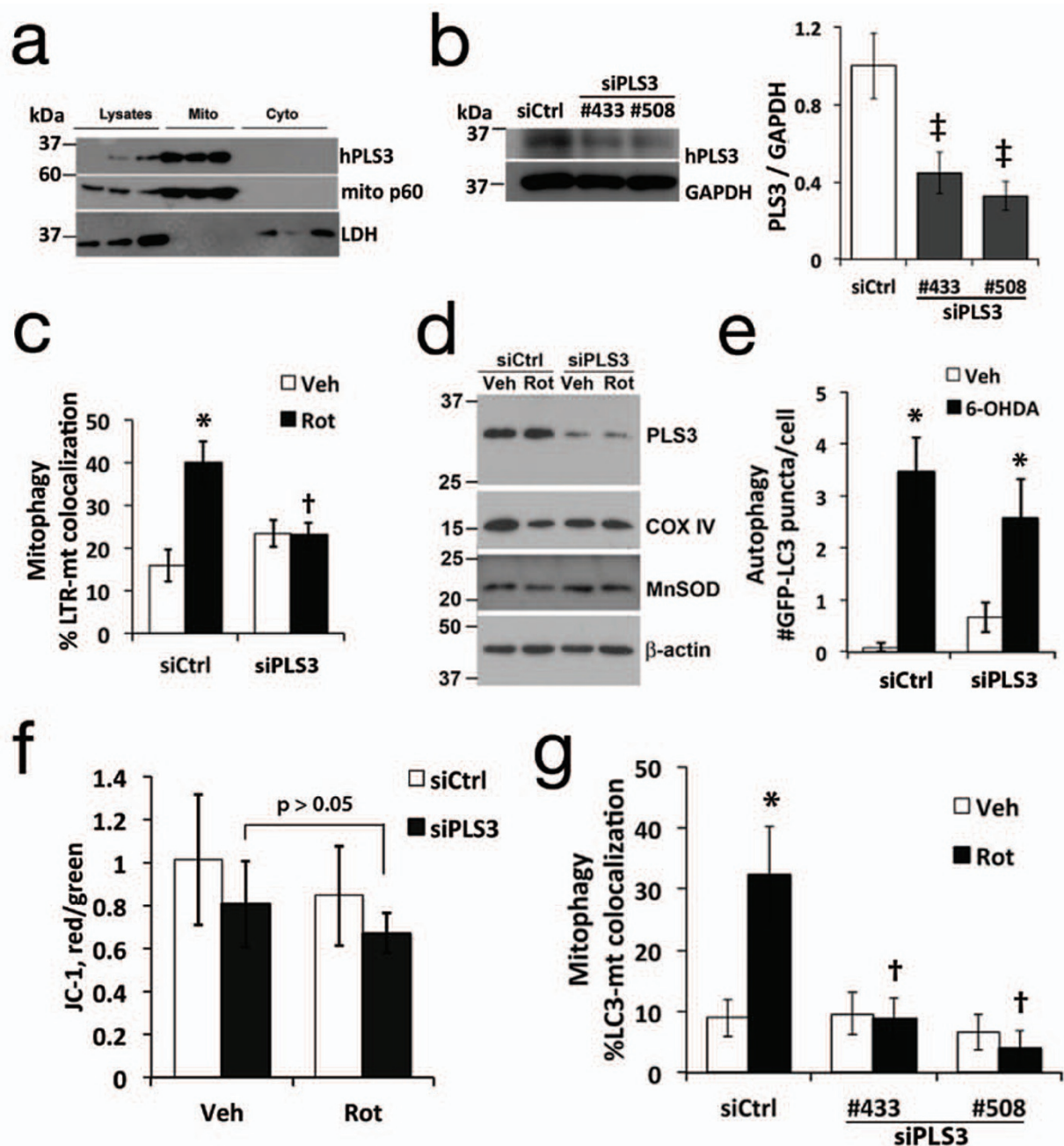
Figure S3 Additional characterization of phospholipid scramblase 3 (PLS3) knockdowns. Mitochondrial and cytosolic fractions from SH-SY5Y cells were immunoblotted for human scramblase-3 (hPLS3), and for the human mitochondrial antigen of 60 kDa (mito-P60) or the cytosolic lactate dehydrogenase enzyme (LDH) as compartment markers **(a)**. SH-SY5Y cells were treated with two siRNAs targeting base pairs 433-453 (#433) or base pairs 508-532 (#508), and the extent of knockdown assessed by immunoblot densitometry **(b)**. n=6, ‡ p<0.05 vs. siCtrl. RNAi knockdown of PLS3 (siPLS3#508) blocks the Rot-induced colocalization of mitochondria with LTR-labeled lysosomes **(c)**. * p<0.05 vs. Veh/siCtrl; † p<0.05 vs. Rot/siCtrl. Western blot analysis of the effects of siPLS3 on Rot-induced decreases in COX IV and MnSOD **(d)**. Effects of PLS3 knockdown on basal and 6-OHDA-elicited GFP-LC3 puncta **(e)**. * p<0.05 vs. respective vehicle treated cells. There were no significant effects of PLS3 knockdown on baseline or rotenone-treated mitochondrial membrane potentials **(f)**. n=8 wells/condition, representative of two independent experiments, no significant changes by ANOVA. The two siRNAs showed equivalent effects on mitophagy elicited by Rot **(g)** or by 6-OHDA (Fig. 3d). * p<0.05 vs. Veh/siCtrl; † p<0.05 vs. Rot/siCtrl.
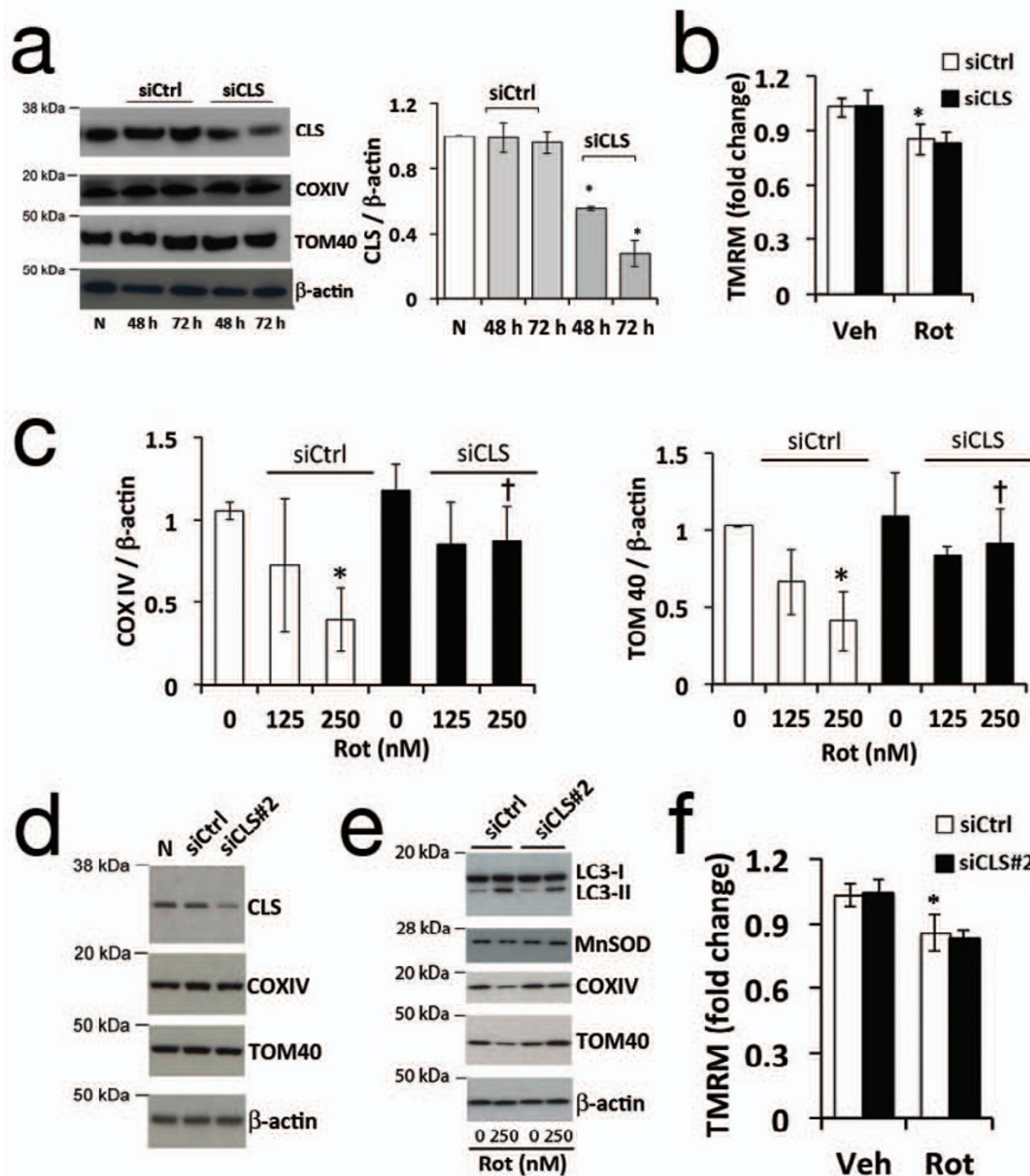
Figure S4 Additional characterization of cardiolipin synthase (CLS) knockdowns. Treatment of primary cortical neurons with siCLS resulted in knockdown of rat CLS without affecting expression of other mitochondrial proteins **(a)**. N=3, mean +/- s.d. * p < 0.05 vs. siCtrl. CLS knockdown had no effects on membrane potential measured by TMRM staining, and did not affect the small, but significant decrease elicited by rotenone **(b)**. N=3, * p < 0.05 vs. Veh. CLS knockdown suppressed the loss of mitochondrial proteins elicited by rotenone as quantified by densitometry **(c)**. N=3; * p <0.05 vs. vehicle; † p < 0.05 vs. respective Rot/siCtrl. See also Fig. 3g-3i for representative blots and additional quantification. A second independent CLS siRNA (siCLS#2) was also effective in reducing CLS expression **(d)** and inhibiting the loss of mitochondrial proteins **(e),** with no effect on baseline or rotenone-treated membrane potentials **(f)**. N=3, * p < 0.05 vs. Veh.
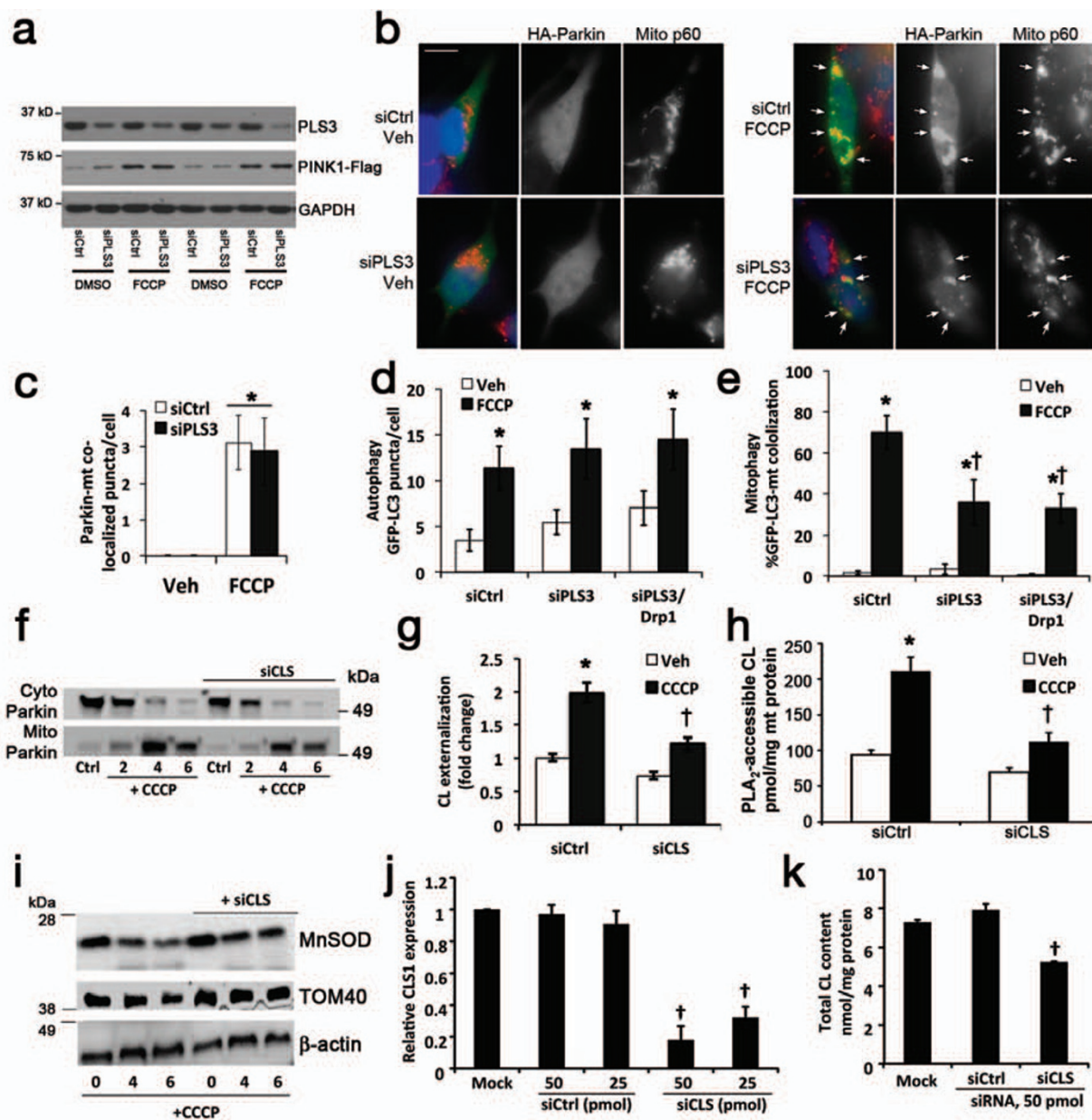
Figure S5 The potential relationship of CL to the FCCP/CCCP-PINK1-Parkin pathway. A previously characterized stable PINK1-3xFlag expressing SH-SY5Y line (#24, Dagda *et al* 2009 Reference 45), was treated with FCCP (2μM x 4 hrs) beginning at 72 h after transfection with siCtrl or siPLS3. Immunoblot analysis confirms PLS3 knockdown, which had no effect on the well-characterized FCCP-induced accumulation of full-length PINK1 **(a)**. SH-SY5Y cells were co-transfected with HA-Parkin and siCtrl or siPLS3, treated with FCCP 72 h later, fixed in paraformaldehyde and immunolabeled for HA (green) and mitochondrial p60 antigen (red). Scale bar: 10μm. FCCP elicited HA-Parkin puncta, all of which colocalized with mitochondrial p60 **(b,** arrows). There were no effects of siPLS3 on basal or FCCP-induced Parkin puncta **(c)**, nor were there effects on FCCP-induced mitochondrial translocation of Parkin analyzed by immunoblot (not shown). *p <0.05 vs. respective Veh-treated cells. While PLS3 knockdown had no effect on FCCP-induced autophagosomes **(d)**, it significantly reduced the

degree of mitophagy elicited by FCCP **(e)**. Overexpression of Drp1 did not rescue the inhibition of mitophagy by PLS knockdown **(e)**, despite promoting significant further mitochondrial fragmentation (not shown). * p<0.05 vs. respective Veh-treated cells; † p<0.05 vs. FCCP/siCtrl. Similarly, in Parkin-expressing HeLa cells, knockdown of CLS (siCLS #S29308) did not block the mitochondrial translocation of Parkin **(f)**. Nevertheless, CCCP treatment did elicit higher levels of CL at the mitochondrial surface, as assessed using both the AnnexinV assay **(g)** and the PLA₂ hydrolysis assay **(h)**, which was inhibited by siCLS. * p<0.05 vs. Veh/siCtrl. † p <0.05 vs. CCCP/siCtrl. CCCP treatment of Parkin-expressing HeLa cells resulted in the loss of mitochondrial proteins MnSOD and TOM40, while RNAi knockdown of CLS partially reduced this loss **(i)**. Representative of 3 independent experiments. Effective knockdown of human CLS was demonstrated in Parkin-transfected HeLa cells at 72h after siRNA treatment **(j),** which was associated with a ~30% decrease in the levels of total CL **(k)**.
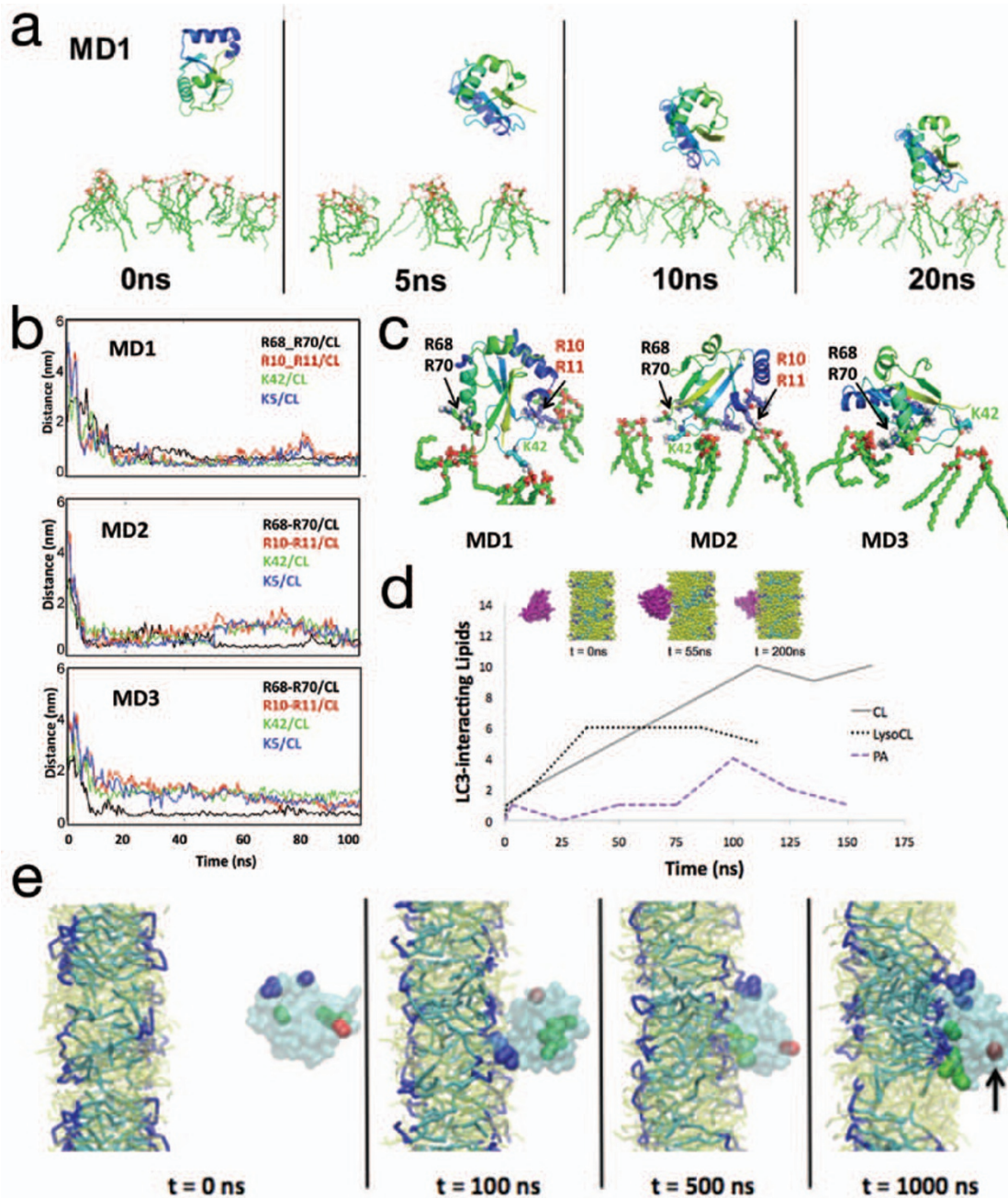
Figure S6 Dynamic modeling of LC3/CL interactions. LC3 and three closest CL molecules in simulation MD1 are shown at four successive snapshots **(a)**. Water, ions and POPC molecules are not shown in the snapshots for clarity. Note that LC3 enters the interaction range (less than 6 Å) of CL within 10 ns in all three simulations. Time evolution of LC3 position **(b)**, monitored as minimum distances between head group atoms on CL and residues R68-R70 (black), R10-R11 (red), K42 (green) or K5 (blue) as observed in each of the three simulations (MD1-3). Magnified snapshots illustrate LC3/CL binding poses with the indicated residues at the end of 50 ns in each of the three simulations **(c)**. For clarity, only those CL molecules which interact with LC3 are illustrated. The LC3 residues interacting with CL are highlighted in stick representation and labeled. The number of CL, PA and LysoCL interacting with LC3 is graphed with time during CGMD simulations **(d)**. Inset snapshots illustrate the simulated interaction of LC3 with a PA-containing bilayer. Color guide: DOPC: yellow; head groups of PA: dark blue; acyl chain of PA: light blue; LC3: purple. CGMD simulation of the interaction of CL with LC3 for 1 μs **(e)**. Snapshots illustrate the simulated interaction of LC3 with a CL-containing membrane using elastic network to preserve the protein structure (Refs. 9-10, SI Note). Note that water, ions and DOPC molecules are not shown for clarity. Color guide: head groups of CL: dark blue sticks, acyl chain of CL: light blue sticks, LC3: cyan (transparent), N-terminus of LC3 (K5, R10-R11): blue spheres, K49, R68-R69-R70: green spheres, Glu117: red sphere). Arrow indicates the C-terminal region involved in lipidation.
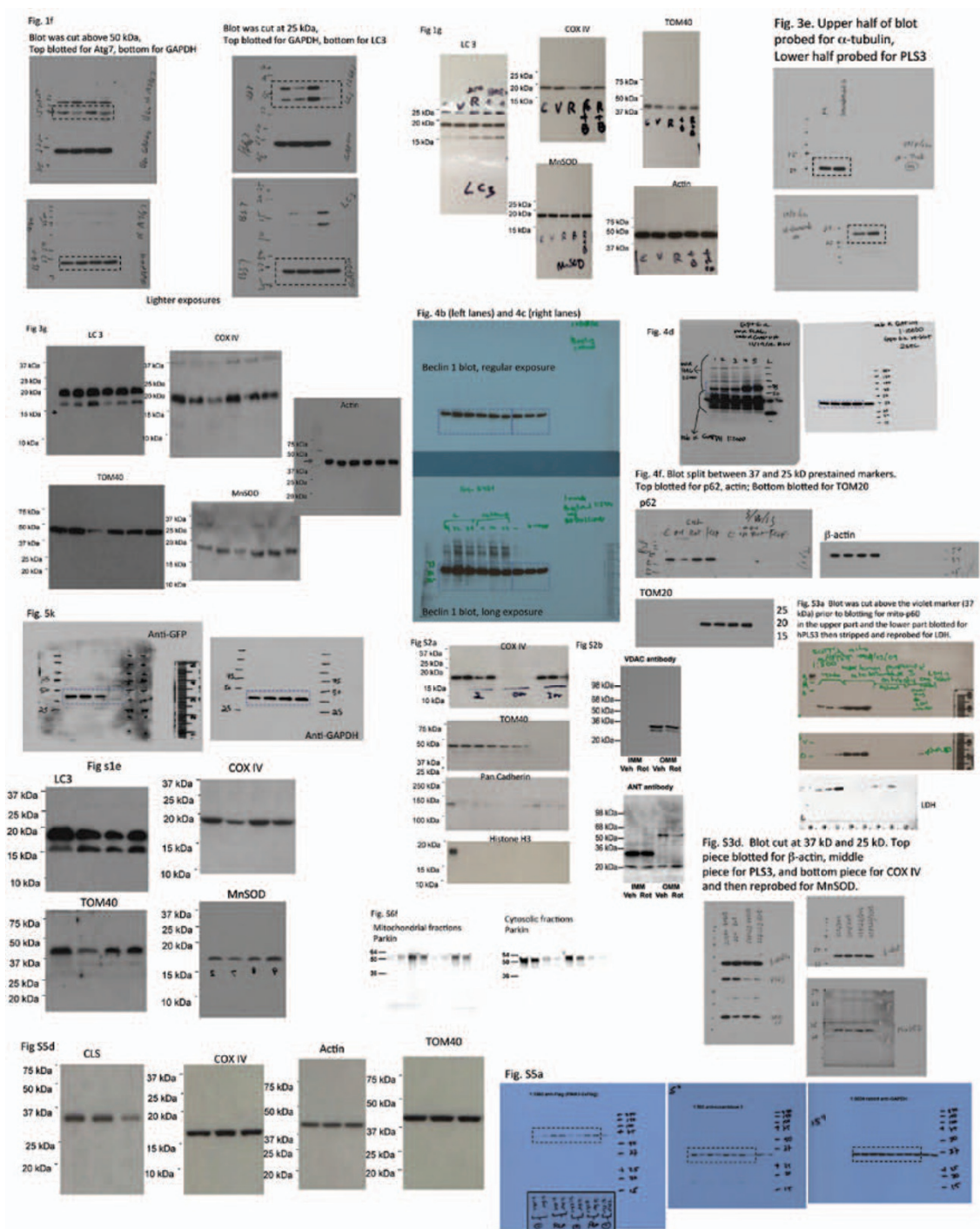
Figure S7 Uncropped western blots. Shown in this figure are all immunoblots from which the multiblot figure panels or insets for Figures 1f, 1g, 3e, 3g, 4b, 4c, 4d, 4f, and 5k were derived. Also shown are key uncropped immunoblots comprising panels in Supplementary Figures S1, S2, S3, and S5.

Table S1. The Rotenone-Treated Cortical Neuron OMM Exhibits a Similar Number and Distribution of CL Species as the Control Neuron IMM.

The m/z values of the CL species for rotenone-treated neuron OMMs and for control neuron IMMs are compared for the 7 major clusters of CL detected. The table displays a similar number and distribution of CL in the OMM in rotenone treated neurons as compared to control IMMs. MS/MS analysis was performed on the major CL species from each cluster, revealing that the major CL species of each cluster from the rotenone-treated OMM was structurally identical to the corresponding species from the control neuron IMM.

CL Species(m/z) in Rotenone-treated cortical neuron OMM

Cluster 1	Cluster 2	Cluster 3	Cluster 4	Cluster 5	Cluster 6	Cluster 7
1372	1396	1422	1446	1474	1498	1522
	1398	1424	1448	1476	1500	1524
	1400	1426	1450	1478	1502	1526
	1402	1428	1452	1480	1504	1528
		1430	1454			
			1456			
			1458			

Fatty acyl chain analysis for main species in OMM after rotenone.
m/z 1372, $(16:1)_3 (18:1)_1$; m/z 1400, $(16:1)_2 (18:1)_2$; m/z 1428, $(16:1)_1 (18:1)_3$; m/z 1456, $(18:1)_4$; m/z 1478, $(18:1)_3 (20:4)_1$; m/z 1502, $(18:0)_1 (18:1)_1 (20:4)_2$; m/z 1526, $(18:1)_2 (20:3)_1 (22:6)_1$.

CL Species(m/z) in control cortical neuron IMM

Cluster 1	Cluster 2	Cluster 3	Cluster 4	Cluster 5	Cluster 6	Cluster 7
1370	1394	1420	1446	1472	1498	1522
1372	1396	1422	1448	1474	1500	1524
1374	1398	1424	1450	1476	1502	1526
	1400	1426	1452	1478	1504	1528
	1402	1428	1454	1480		
		1430	1456	1482		
		1432	1458			
			1460			

The fatty acyl analysis for main species in IMM control
m/z 1372, $(16:1)_3 (18:1)_1$; m/z 1400, $(16:1)_2 (18:1)_2$; m/z 1428, $(16:1)_1 (18:1)_3$; m/z 1456, $(18:1)_4$; m/z 1478, $(18:1)_3 (20:4)_1$; m/z 1502, $(18:0)_1 (18:1)_1 (20:4)_2$; m/z 1526, $(18:1)_2 (20:3)_1 (22:6)_1$.

Table S2. Residues of LC3 interacting with CL as evidenced by Coarse-Grained Molecular Dynamics simulation. The data reflect one of the prototypical simulations found in three out of four performed CGMD experiments. The first contact involves N-terminal residues F7-K8-Q9-R10-R11 [Note overlap with the favored docked conformation of F7-R10-R11 (Figure 5c,e)]. These residues stay in contact throughout the rest of the simulation. While additional electrostatic interactions form subsequently, a hydrophobic contribution develops through involvement of V33-I34-V46-F52-L53-I67 at 100ns, which is further expanded with the addition of V17-V20- L22-I31-I35-Y38-L47-V54-I64-I66-L71-F79-F80-L82-L83-I95-F108-Y110 at 150ns. A distance of < 5Å was used to identify interacting molecules **Bold**: residues that contact the bilayer after 50ns. Underlined: residues in contact after 100ns.

Time (ns)	Residues	Number of Residues
40	--	0
50	**F7-K8-Q9-R10-R11**	5
100	K5-**F7**-**Q9-R10-R11**-E14-<u>H27</u>-<u>T29</u>-<u>K30</u>-P32-<u>V33</u>-<u>I34</u>-R37-P45-V46-<u>K49</u>-<u>T50</u>-<u>F52</u>-<u>L53</u>-I67-<u>R68</u>	21
150	**F7-Q9-R10-R11**-V17-V20-R21-L22-<u>H27</u>-<u>T29</u>-<u>K30</u>-I31-<u>V33</u>-<u>I34</u>-I35-Y38-K42-L47-<u>K49</u>-<u>T50</u>-<u>F52</u>-<u>L53</u>-V54-N59-I64-I66-<u>R68</u>-L71-F79-F80-L82-L83-I95-F108-Y110	35

Table S3. Mammalian LC3B aligned with Atg8 homologs from different species.
Alignment of LC3B using CLUSTAL Omega Algorithm.

*conserved amino acid residues.
Highlighted yellow are key residues for the thermodynamically preferred cardiolipin-binding site on LC3, as identified by docking analysis (Fig. 5c-e). Conservative substitutions are shown in grey. Contact residues for an alternative cardiolipin binding orientation are highlighted blue. Residues implicated in both conformations are shown in green.

```
Human LC3       mpsektfkqrrtfeqrvedvrlireqhptkipviierykgekqlpvldktkflvpdhvnm
Rat LC3         mpsektfkqrrsfeqrvedvrlireqhptkipviierykgekqlpvldktkflvpdhvnm
Mouse LC3       mpsektfkqrrsfeqrvedvrlireqhptkipviierykgekqlpvldktkflvpdhvnm
Bovine LC3      mpsektfkqrrtfeqrvedvrlireqhptkipviierykgekqlpvldktkflvpdhvnm
Zebrafish       mpsektfkqrrtfeqrvedvrlireqhpnkipviierykgekqlpildktkflvpdhvnm
C. elegans      --mkwaykeennfekrraegdkirrkypdripvivekapk-sklhdldkkkylvpsdltv
Drosophila      mdmnyqykkdhsfdkrrnegdkirrkypdrvpvivekapk-tryaeldkkkylvpadltv
Yeast Atg8      --mkstfkseypfekrkaeseriadrfknripvicekaek-sdipeidkrkylvpadltv
Human GABARAP   --mkfvykeehpfekrrsegekirkkypdrvpvivekapk-arigdldkkkylvpsdltv
Human GATE-16   --mkwmfkedhslehrcvesakirakypdrvpvivekvsg-sqivdidkrkylvpsditv
                   *         *         *       *** *            ** * ***

Human LC3       selikiirrrlqlnanqafflllvnghsmvsvstpisevyesekdedgflymvyasqetfg
Rat LC3         selikiirrrlqlnanqafflllvnghsmvsvstpisevyeserdedgflymvyasqetfg
Mouse LC3       selikiirrrlqlnanqafflllvnghsmvsvstpisevyeserdedgflymfyasqetfg
Bovine LC3      selikiirrrlqlnanqafflllvnghsmvsvstpicevyesekdedgflymvyasqetfg
Zebrafish       selikiirrrlqlnsnqafflllvnghsmvsvstaisevyererdedgflymvyasqetfg
C. elegans      gqfyflirkriqlrpedalffffvnnv-ipqtmttmgqlyqdhheedlflyiaysdesvyg
Drosophila      gqfyflirkrinlrpddalffffvnnv-ipptsatmgalyqehfdkdyflyisytdenvyg
Yeast Atg8      gqfvyvirkrimlppekaififvndt-lpptaalmsaiyqehkdkdgflyvtysgentfg
Human GABARAP   gqfyflirkrihlraedalffffvnnv-ipptsatmgqlyqehheedfflyiaysdesvyg
Human GATE-16   aqfmwiirkriqlpsekaiflfvdkt-vpqssltmgqlyekekdedgflyvaysgentfg
                    ** *  *  *    * * *            *     * *** *         *
```

Supplemental Information Note

To supplement the molecular docking predictions of CL-binding pockets at the LC3 surface, facilitating identification of key residues for mutagenesis, we used molecular modeling to simulate the binding of human LC3B to PC bilayer membranes containing CL or PA (Supplementary Fig. S6). Three independent all-atom molecular dynamics (MD) simulations (MD1-MD3) of 100 ns each were performed for a system of ~150,000 atoms at full atom resolution, including LC3, nine CLs embedded in a lipid bilayer of POPC molecules and explicit water molecules. In all three runs, LC3, originally placed ~20 Å away from the bilayer surface, reoriented and translocated towards the bilayer surface to rapidly interact with CL (Supplementary Fig. S6a). The significant displacement of LC3 was driven by strong electrostatic interactions between the negatively charged CL head groups and positively charged residues on LC3. Analysis of the minimum distance between LC3 residues and any CL atom in MD1, MD2 and MD3 simulations with time suggested that the interactions of LC3 with CL involved several conserved positively charged residues on the LC3 surface (Supplementary Fig. S6b). LC3 appeared to simultaneously bind to three CLs in MD1 and MD2 (Supplementary Fig. S6c), via the positively charged residues R68-R70, R10-R11, K42 and K5, and to two CLs in MD3 primarily via residues R68-R70 with transient involvement of K42 (Supplementary Fig. S6c). In three control simulations with the lipid bilayer devoid of CL, LC3 was 3-4 times slower in its initial approach to the bilayer. A longer time scale (1 µs) examination of LC3-CL interactions was performed using coarse-grained MD (CGMD). The overall comparison of the interactions of LC3 with the lipid bilayer in the presence or absence of CL (three 1 µs simulations) suggests that the presence of CL facilitates more rapid diffusion towards bilayers followed by stronger, more specific interactions (Supplementary Fig. S6d). CGMD trajectories suggest that LC3 fluctuates near PA-containing bilayer surfaces (Figure S6d). In contrast, the interaction of LC3 with the CL-containing bilayer appeared to be stabilized by recruitment of additional interaction sites, particularly for CL bearing four acyl chains, as observed experimentally (Fig. 5b). The three CGMD simulations indicated the involvement of residues K5, R10 and R11 in the initial interactions with the CL-containing bilayer, with recruitment of residues R68-R70 and K49 (Supplementary Fig. S6e and Table S2).

Although the simulations are likely to provide insights into early recognition events rather than thermodynamically stable binding conformations, both full-atomic and CG methods implicated residues in two regions - K5, R10-R11 and R68-R70 – in early interactions of LC3 with CL containing membranes. Notably, the C-terminal region of LC3, which becomes cross-linked to autophagosome membranes, remained exposed throughout the simulation (Supplementary Fig. S6e, arrow), compatible with its proposed bridging role.

Methods for Molecular Dynamics Simulations

All-atom Molecular Dynamics (MD) simulations were performed for the system consisting of LC3, CL molecules in the presence of explicit 1-palmitoyl-2-oleoyl-sn-glycero-3-phosphocholine POPC (lipid) molecules and water. The published high resolution (2.05 Å) structure of LC3 (1UGM) was used[1]. The coordinates for CL molecules were derived from the crystallographically resolved cytochrome *c* oxidase complex structure (PDB id: 1V54)[2], which included two bound CL molecules. A pre-equilibrated POPC bilayer, consisting of 400 lipid molecules was used. Nine CLs were inserted randomly into the POPC bilayer, and POPC molecules located within 2.0 Å of each CL was removed. This system was solvated and energy minimized, followed by an

equilibration of 5 nanoseconds (ns), to allow the lipids to pack around the CL. The resulting mixed bilayer was used as the input structure for productive runs, in which LC3 was placed at a distance of ~20 Å from the bilayer surface. This system was also energy minimized and equilibrated for 1 ns, during which the protein was restrained. The entire equilibrated system of LC3, CL, POPC and water molecules and counter ions consisted of 149,356 atoms. The system was used to generate three simulation trajectories of 100 ns each (MD1, MD2 and MD3) with different initial velocities. The software GROMACs[3] was used to simulate the system.

The Coarse-Grained MD (CGMD) simulations of lipid bilayer systems were carried out by coarse-graining 4 atoms to one bead using the MARTINI force field developed by Marrink et al.[4]. In this method, the equilibrium distance between beads in the acyl chain of a lipid is 0.47nm, but the force constants are weak, permitting motion. The lipid bilayer was composed of DOPC and varying additional lipids each at ~20% (CL, PA, monolyso-CL, dilyso-CL) Three CGMD simulations, employing different initial velocities with identical initial configurations, were performed to study interaction of LC3 and CL-containing bilayer in addition to three control simulations using the bilayer without CL. CGMD simulations were performed using the GROMACS v. 4.5.4 MD package. Initially, the system was minimized for 20 ps, before 0.2 ns NPT ensemble equilibration followed by a 0.2ns NVT ensemble equilibration. Each MD run was carried out for 1 μs. A 20 fs time step was used to integrate the equations of motion. Non-bonded interactions have a cutoff distance of 1.2nm. The long-range Coulomb interactions were calculated via the particle-mesh Ewald method[5]. The dimensions of the simulation box was 20x7x7 nm^3. Temperature and pressure were controlled using the Nosé-Hoover[6] and Berendsen[7] algorithms, respectively. Simulations were run at 300K and at 1atm during NPT runs. For all CG simulations, visualization and analysis were performed using the VMD v. 1.9 visualization software[8], using elastic network to preserve the protein structure[9, 10]. The C-terminal region of LC3 was tracked by following Glu117, the last residue in the 1UGM structure, throughout the simulation.

1. Sugawara, K. *et al.* The crystal structure of microtubule-associated protein light chain 3, a mammalian homologue of Saccharomyces cerevisiae Atg8. *Genes Cells* **9**, 611-618 (2004).
2. Tsukihara, T. *et al.* The low-spin heme of cytochrome c oxidase as the driving element of the proton-pumping process. *Proceedings of the National Academy of Sciences of the United States of America* **100**, 15304-15309 (2003).
3. Van Der Spoel, D. *et al.* GROMACS: fast, flexible, and free. *Journal of computational chemistry* **26**, 1701-1718 (2005).
4. Marrink, S.J., Risselada, H.J., Yefimov, S., Tieleman, D.P. & de Vries, A.H. The MARTINI force field: coarse grained model for biomolecular simulations. *The journal of physical chemistry. B* **111**, 7812-7824 (2007).
5. Essman, U. *et al.* A smooth particle mesh Ewald method. *J. Chem. Phys.* **103**, 8577-8593 (1995).
6. Evans, D.J. & Holian, B.L. The Nose-Hoover thermostat. *Journal of Chemical Physics* **85**, 4069-4074 (1985).
7. Berendsen, H.J.C., Postma, J.P.M., van Gunsteren, W.F., DiNola, A. & Haak, J.R. Molecular dynamics with coupling to an external bath. *Journal of Chemical Physics* **81**, 3683-3690 (1984).
8. Humphrey, W., Dalke, A. & Schulten, K. VMD: visual molecular dynamics. *Journal of molecular graphics* **14**, 33-38, 27-38 (1996).

9. Arnarez, C., Mazat, J.P., Elezgaray, J., Marrink, S.J. & Periole, X. Evidence for cardiolipin binding sites on the membrane-exposed surface of the cytochrome bc1. *Journal of the American Chemical Society* **135**, 3112-3120 (2013).
10. Periole, X., Cavalli, M., Marrink, S.-J. & Ceruso, M.A. Combining an elastic network with a coarse-grained molecular force field: structure, dynamics, and intermolecular recognition. *J Chem Theory Comput* **5**, 2531-2543 (2009).